The Astronomical Journal, 168:69 (18pp), 2024 August https://doi.org/10.3847/1538-3881/ad543f

LIGHTS. Survey Overview and a Search for Low Surface Brightness Satellite Galaxies

Dennis Zaritsky[1], Giulia Golini[2,3], Richard Donnerstein[1], Ignacio Trujillo[2,3], Mohammad Akhlaghi[4], Nushkia Chamba[5], Mauro D'Onofrio[6], Sepideh Eskandarlou[4], S. Zahra Hosseini-ShahiSavandi[6], Raúl Infante-Sainz[4], Garreth Martin[7], Mireia Montes[2,3], Javier Román[3,8], Nafise Sedighi[9], and Zahra Sharbaf[2,3]
[1] Steward Observatory and Department of Astronomy, University of Arizona, 933 N. Cherry Avenue, Tucson, AZ 85721, USA; dennis.zaritsky@gmail.com
[2] Instituto de Astrofśica de Canarias, c/ Vía Láctea s/n, 38205 La Laguna, Tenerife, Spain
[3] Departamento de Astrofísica, Universidad de La Laguna, 38206 La Laguna, Tenerife, Spain
[4] Centro de Estudios de Física del Cosmos de Aragón (CEFCA), Plaza San Juan, 1, E-44001, Teruel, Spain
[5] NASA Ames Research Center, Moffett Field, CA 94035, USA
[6] Department of Physics and Astronomy, University of Padua, Vicolo Osservatorio 3, 35122 Padova, Italy
[7] School of Physics and Astronomy, University of Nottingham, University Park, Nottingham NG7 2RD, UK
[8] Kapteyn Astronomical Institute, University of Groningen, PO Box 800, 9700 AV Groningen, The Netherlands
[9] Department of Physics, Yazd University, 8915818411, Yazd, Iran
Received 2024 February 29; revised 2024 June 2; accepted 2024 June 3; published 2024 July 11

Abstract

We present an overview of the LBT Imaging of Galactic Halos and Tidal Structures survey, which currently includes 25 nearby galaxies that are on average ∼1 mag fainter than the Milky Way, and a catalog of 54 low central surface brightness ($24 < \mu_{0,g}/\mathrm{mag\,arcsec^{-2}} < 28$) satellite galaxy candidates, most of which were previously uncatalogued. The depth of the imaging exceeds the full 10 yr depth of the Rubin Observatory's Legacy Survey of Space and Time. We find, after applying completeness corrections, rising numbers of candidate satellites as we approach the limiting luminosity ($M_r \sim -8$ mag) and central surface brightness ($\mu_{0,g} \sim 28$ mag arcsec^{-2}). Over the parameter range we explore, each host galaxy (excluding those that are in overdense regions, apparently groups) has nearly four such candidate satellites to a projected radius of ∼100 kpc. These objects are mostly just at or beyond the reach of spectroscopy unless they are H I rich or have ongoing star formation. We identify three, possibly four, ultra-diffuse satellite galaxies (effective radius >1.5 kpc). This incidence rate falls within expectations of the extrapolation of the published relationship between the number of ultra-diffuse satellite galaxies and host halo mass. Last, we visually identify 12 candidate satellites that host a nuclear star cluster (NSC). The NSC occupation fraction for the sample (12/54) matches that published for satellites of early-type galaxies, suggesting that the parent's morphological type plays at most a limited role in determining the NSC occupation fraction.

Unified Astronomy Thesaurus concepts: Companion galaxies (290); Low surface brightness galaxies (940); Dwarf galaxies (416); Galaxy stellar halos (598)

1. Introduction

Galaxy outskirts, with their long dynamical times, retain the vestiges of their tumultuous formation history—a history that is central to the now-standard, hierarchical picture of galaxy formation at the heart of the ΛCDM model (G. R. Blumenthal et al. 1984; M. Davis et al. 1985); a history that results in testable predictions for the total stellar debris field (e.g., A. S. Font et al. 2011; N. C. Amorisco 2017; A. Merritt et al. 2020), the phase-space signatures of accretion events (J. S. Bullock & K. V. Johnston 2005; K. V. Johnston et al. 2008; A. P. Cooper et al. 2010; G. Martin et al. 2022), and the surviving population of gravitationally bound satellite galaxies (Y.-Y. Mao et al. 2021, and references therein); and a history that is manifested most clearly in the deepest possible images of galaxy halos (surface brightnesses limits >30 mag arcsec^{-2}; K. V. Johnston et al. 2008).

The hierarchical structure formation scenario successfully reproduces a myriad of observations and is arguably one of the triumphs of cosmology, but comparison at galaxy scales and below can be problematic (D. H. Weinberg et al. 2015). Interpreting the apparent failings is complicated by the complex details of the baryonic physics and its effects, as well as by the unknown nature of dark matter. Nevertheless, a full accounting of the satellite mass function is now understood to provide a key test of the models, a possible path to learning more about both the effects of baryonic physics at these scales and the nature of dark matter, and motivation for numerous independent studies (e.g., M. Geha et al. 2017; H. S. Park et al. 2017, 2019; C. Xi et al. 2018; O. Müller & H. Jerjen 2020; S. G. Carlsten et al. 2021; A. Bianca Davis et al. 2021; Y.-Y. Mao et al. 2021; A. Karunakaran et al. 2021; I. M. E. Santos-Santos et al. 2022; M. Nashimoto et al. 2022; J. Li et al. 2023; H. Goto et al. 2023).

Satellite galaxies represent the survivors of the accretion process, while the dispersed stars within the halos testify to the less fortunate. This interpretation is confirmed for the halo of our own galaxy, where $\gtrsim$95% of all halo stars outside of surviving satellite galaxies are traced back to specific progenitor satellite galaxies (R. P. Naidu et al. 2020). Among nearby galaxies, there appears to be a wide variety in the amount of diffuse stellar debris that comprises the stellar halo (E. Sola et al. 2022), including some galaxies with almost no stellar halo (P. G. van Dokkum et al. 2014). Despite theoretical expectations of significant scatter in stellar halo properties (A. P. Cooper et al. 2010; G. Martin et al. 2022), the large

variation observed may be in tension with the standard model (A. Merritt et al. 2016, 2020).

Our Large Binocular Telescope (LBT) Imaging of Galactic Halos and Tidal Structures (LIGHTS) survey is motivated by a desire to establish the range of stellar halo properties and test the basics of the galaxy formation scenario. We aim to provide the best possible measurements of the diffuse halo stellar light for as large a sample of nearby galaxies as possible. Our focus is therefore on reaching as faint a surface brightness limit as possible, while retaining the highest possible angular resolution with which to classify and mask contaminating sources. We introduced the survey in I. Trujillo et al. (2021) by presenting and discussing the data for our first galaxy (NGC 1042). We demonstrated there how LIGHTS images could impact our understanding of stellar halos.

Here, we present our current sample of 25 galaxies and provide an overview of the sample selection and data processing, while also presenting results regarding the relation between the low surface brightness satellite populations and their hosts. In short order, we will also be presenting a determination of the point-spread function in the images to extremely large angular radii (N. Sedighi et al. 2024, in preparation), which is essential in assessing the scattered light across the image, and the generation of object catalogs (S. Z. Hosseini-Shahisavandi et al. 2024, in preparation). Both of these are critical components in making the survey as scientifically useful as possible. As stressed in our introductory paper, LIGHTS is a well-matched precursor to the Legacy Survey of Space and Time (LSST), to be completed by the Vera C. Rubin observatory in somewhat over a decade, and so it also serves as a guide on what to expect from that tremendous resource.

As just mentioned, our focus here is on low surface brightness (LSB) satellite candidates (central surface brightness in the g-band, i.e., $\mu_{0,g} > 24\,\mathrm{mag\,arcsec^{-2}}$). We refer to our cataloged satellite galaxies as candidates because they are not yet confirmed to be at the same distance as the apparent host. The surface brightness boundary is artificial, but does roughly correspond to the types of systems that are now being found in large numbers but were previously seen as rare (e.g., P. G. van Dokkum et al. 2015; J. Koda et al. 2015). We adapt the methodology used by D. Zaritsky et al. (2019, 2021, 2022, 2023), which was specifically designed to identify LSB galaxies in Legacy Survey images (A. Dey et al. 2019) beyond the local flow field.

The resulting catalog from LIGHTS images provides information on the nature of the satellite galaxy population at the limits of surface brightness and total luminosity that can be probed currently from the ground in galaxies well outside the Local Group, and it complements Local Group or nearby galaxy studies by providing measurements for a larger set of parent galaxies. These results will eventually be matched to those on the diffuse halo light for these same galaxies, to provide a complete accounting of the stellar halos of galaxies.

In complementing our presentation here of the LIGHTS survey sample with some example results, we focus on two extremes of surface brightness properties. First, we discuss ultra-diffuse galaxies (UDGs), which are those LSB satellites that have effective radii larger than 1.5 kpc ($r_e > 1.5$ kpc). These galaxies are of interest because they include some of the most massive of the LSB galaxy population (P. van Dokkum et al. 2017; D. Zaritsky 2017). Our satellite candidate catalog enables tests of previous results that use different data, methodology, and parent galaxy type (e.g., H. S. Park et al. 2017; S. G. Carlsten et al. 2021; M. Poulain et al. 2021; H. Goto et al. 2023). For example, we will use our catalog to test the extrapolation of the relationship between the number of UDGs and parent host halo mass (R. F. J. van der Burg et al. 2016; J. Roman & I. Trujillo 2017; P. E. Mancera Piña et al. 2019; A. Karunakaran & D. Zaritsky 2023; H. Goto et al. 2023). Second, we discuss the incidence of high surface brightness central clusters (nuclear star clusters; NSCs) found in some LSB galaxies. The origin of NSCs remains in question (N. Neumayer et al. 2020), and their presence in LSB galaxies poses additional challenges to any formation scenario (M. Lambert et al. 2024). Here, we explore whether there is evidence for a dependence on the incidence of NSCs in satellite galaxies with parent galaxy morphological type.

This paper is structured as follows: in Section 2, we present and describe the LIGHTS sample and the LIGHTS data reduction procedure through to the generation of final image mosaics. In Section 3, we describe the modifications to the D. Zaritsky et al. (2023) pipeline, our recovery of LSB satellite galaxy candidates, and our estimation of the sample completeness. In Section 4, we present the basic properties of the candidate satellite sample, such as the number of satellites per parent and the number of UDGs. In Section 5, we compare these results to those of other studies. In Section 6, we discuss our results for the number of UDGs per host halo mass relative to the trend observed for more massive host halos and the subsample of nucleated LSB satellite candidates. Magnitudes are provided in the AB system (J. B. Oke 1964; J. B. Oke & J. E. Gunn 1983).

2. Sample and Data Reduction

2.1. The Target Sample

The LIGHTS project aims primarily to study the stellar halo structures of nearby disk galaxies. We set our target selection criteria for reasons based on the scientific aims of the survey, such as the ability to differentiate between extended stellar disk and halo components, and on pragmatic ones, such as the camera's field of view. We adopt the following selection criteria (with specific exceptions noted below): (1) decl. $> -10°$ to allow for relatively low air-mass observations (air mass < 1.4) from the LBT (at latitude $\sim 32°$); (2) an angular diameter that lies between $4'$ and $10'$ as measured by D_{26}, the diameter corresponding to the r-band $26\,\mathrm{mag\,arcsec^{-2}}$ isophote, to reasonably match the field of view of the Large Binocular Cameras (LBC) instrument (see Section 2.2); (3) an axis ratio, b/a, <0.8 to provide geometric contrast between a stellar halo and an extended disk component; (4) a Galactic reddening, $E(B-V)$, <0.04 as measured by D. J. Schlegel et al. (1998) to avoid regions of high Galactic extinction; (5) a redshift, z, less than 0.006 (closer than ~ 26 Mpc) to limit the study to nearby galaxies and provide us with high physical resolution (corresponding to $\sim 30\,\mathrm{pc\,pixel^{-1}}$ at the native image resolution and $100\,\mathrm{pc\,pixel^{-1}}$ in the binned images we will use for detecting low surface brightness satellite candidates; Section 3); and (6) an absence of nearby projected bright stars (first determined using an automated pass through the Yale Bright Star Catalog (D. Hoffleit & W. H. J. Warren 1995) to search for stars within $1°$ and then a visual examination based on experience as the program progressed). The data we use to

make this selection (Table 1) are drawn from the Sienna Galaxy Catalog 2020 (J. Moustakas et al. 2023), which provides photometric measurements of galaxies of large angular extent from the Legacy Survey data (A. Dey et al. 2019), and ancillary data drawn from the Hyperleda Extragalactic Database[10] (D. Makarov et al. 2014), except for the distances (see below), and the number of identified LSB candidate satellites, $N_{\rm LSB}$, and ultra-diffuse galaxies, $N_{\rm UDG}$, which we measure here. The number of galaxies projected within 100 kpc and having a measured recessional velocity within 500 km s^{-1} of the target galaxy in the Hyperleda database are tabulated as $N_{\rm LEDA}$. The radial cut matches the projected radii probed by the LIGHTS images, and the velocity cut is set to include both bound satellites and potential group members.

We adopt published distances from studies utilizing standard candles (SNe, TRGB, and Cepheids), scaling relations (Tully–Fisher), and detailed cosmological flow modeling. We chose which distance measurements to adopt based on our own evaluation of the relative merits, and the selected references are noted in Table 1 as $D_{\rm ref}$. Distance estimates, in particular at distances where the peculiar velocity is not $\ll$ than the Hubble flow velocity, can be highly uncertain. In extreme cases, literature studies can disagree on the distance by as much as a factor of two. The notable example within our sample is NGC 1042, for which our adopted distance of 13.5 ± 2.6 Mpc is markedly different than that presented in a separate study (20.0 ± 1.6 Mpc; S. Danieli et al. 2020). Although this difference has significant repercussions on certain questions of great interest (e.g., I. Trujillo et al. 2019; S. Danieli et al. 2020) and the choice of distance impacts the physical parameters we present for our satellite candidates, it does not significantly affect the results presented here from our overall sample. Nevertheless, uncertainties in the derived physical parameters of our candidates, even for galaxies other than NGC 1042, are dominated by distance uncertainties.

We violate our selection criteria on occasion, as is evident in Table 1. Specifically, we exceed the D_{26} criterion by including NGC 2903, NGC 5033, and NGC 5907, which all have $D_{26} > 10'$ (12.82, 11.53, and 21.′16, respectively). The angular sizes of these make the images more difficult to reduce, even when our dithering steps are larger. Two of these are included because they are part of an earlier leading study of stellar halos (NGC 2903 and NGC 5907; A. Merritt et al. 2016) and so are valuable for comparison. We also violate the $b/a < 0.8$ criterion by including NGC 1042, NGC 3351, NGC 3486, and NGC 3596 (0.87, 0.89, 0.87, and 0.91, respectively). Two of these (NGC 1042 and NGC 3351) are included because they are also in the A. Merritt et al. (2016) study. Regarding the remaining galaxies that violate the criteria and are not in an earlier study, we included them due to a shortage of more suitable targets.

In Figure 1, we show that the sample consists of galaxies that are morphologically similar to the Milky Way but have a median magnitude that is ∼1 mag fainter (−20.6). The sample, as a whole, cannot be characterized as Milky Way analogs, although a subsample of ∼5 galaxies (NGC 3675, NGC 3953, NGC 4321, NGC 5907, and NGC 5033) can be defined as such if one desires a closer comparison to the MW satellite system.

[10] http://leda.univ-lyon1.fr/

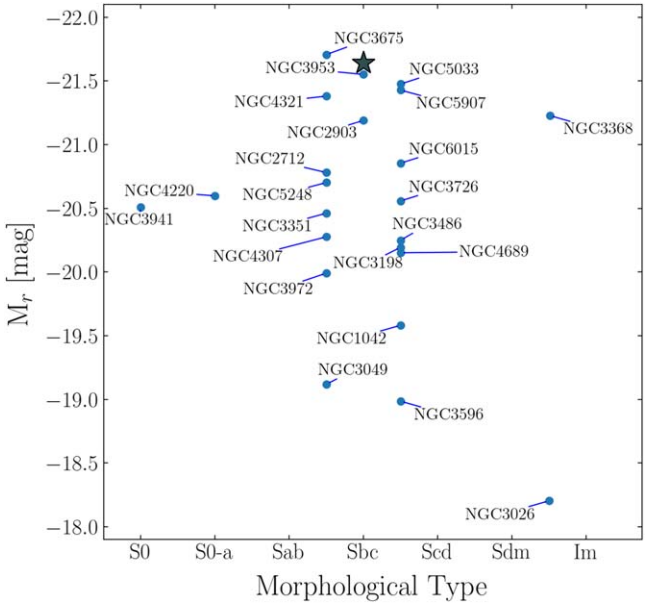

Figure 1. The LIGHTS sample to date in the morphology-absolute magnitude space. The star represents the Milky Way for comparison, with an adopted absolute magnitude of $M_r = -21.64$ (J. Bland-Hawthorn & O. Gerhard 2016) and a morphological classification of Sbc (P. W. Hodge 1983; R. C. J. Kennicutt 2001).

2.2. LIGHTS Processing Overview

We obtained ultra-deep observations of LIGHTS targets using the LBT and both channels (blue and red) of the LBC simultaneously (E. Giallongo et al. 2008). The observations presented here were carried out during Director Discretionary Time (DDT; P.I. D'Onofrio) and standard allocated time (P.I. Zaritsky) beginning in 2020 October through the first half of 2023. Each of the two LBC cameras consist of four CCDs, with a pixel scale of 0.″224 pixel^{-1}, covering an approximate area of 7.′8 × 17.′6 per CCD, with ∼18″ wide gaps between the chips. The combined field of view for each LBC camera is roughly 23′ × 25′. We used the *g*-SLOAN filter on the LBC Blue camera and the *r*-SLOAN filter on the LBC Red camera optimized for the wavelength ranges 3500 Å–6500 Å and 5500 Å–1 μm, respectively.

Attentive observing and data reduction procedures are required to address different and complex observational challenges such as scattered light, strongly saturated stars, and ghosts. Furthermore, to obtain images in which low surface brightness features are reliable (i.e., limiting surface brightness of $\mu_g \sim 31$ mag arcsec^{-2}, 3σ in a 10″ × 10″ box), accurate flat-field estimation and careful treatment of the sky background are integral. The latter task in particular is challenging because observational conditions, like the air mass and light cloud coverage, change throughout the night. To mitigate these issues, we apply a specific observational strategy involving a dithering pattern using ten 180 s exposures per sequence (I. Trujillo et al. 2021), with which the total exposure time is built up, and an optimized data reduction pipeline based on extensive prior experience (e.g., I. Trujillo & J. Fliri 2016). The data reduction pipeline relies on GNU Astronomy Utilities (Gnuastro; M. Akhlaghi & T. Ichikawa 2015; M. Akhlaghi 2019). Below, we provide an overview of the key stages in this process. Further details will be provided by G. Golini et al. (2024, in preparation).

Table 1
LIGHTS Target Galaxies

Name	R.A.	Decl.	m_g (mag)	m_r (mag)	D (Mpc)	σ_D (Mpc)	$D26$ ($'$)	$E(B-V)$	b/a	z	Morph	$N_{\rm LSB}$	$N_{\rm UDG}$	$N_{\rm LEDA}$	$D_{\rm ref}$
NGC1042	40.09986	−8.43354	11.64	11.07	13.5	2.6	5.47	0.029	0.87	0.0046	SABc	7	0	6	(1)
NGC2712	134.87698	44.91390	12.33	11.62	30.2	2.0	4.49	0.020	0.54	0.0061	SBb	2	0	0	(2)
NGC2903	143.04212	21.50083	9.52	8.81	10.0	2.5	12.82	0.031	0.52	0.0019	Sbc	0	0	1	(2)+(3)+(4)
NGC3026	147.73071	28.55111	13.32	12.79	15.8	2.0	4.64	0.021	0.26	0.0049	SBm	0	0	0	(5)
NGC3049	148.70652	9.27109	12.95	12.31	19.3	0.2	4.34	0.038	0.50	0.0050	SBb	0	0	1	(3)
NGC3198	154.97897	45.54962	10.95	10.36	12.9	0.1	9.57	0.120	0.36	0.0022	Sc	0	0	1	(3)
NGC3351	160.99042	11.70381	10.29	9.53	10.0	0.3	7.58	0.028	0.89	0.0026	Sb	0	0	1	(6)
NGC3368	161.69058	11.81994	9.79	9.02	11.2	0.5	9.54	0.025	0.75	0.0030	Sab	4	0	0	(6)
NGC3486	165.09945	28.97514	11.00	10.42	13.6	0.1	6.30	0.022	0.87	0.0023	Sc	1	0	0	(4)
NGC3596	168.77586	14.78702	11.85	11.28	11.3	1.1	3.99	0.024	0.91	0.0040	SABc	1	0	2	(6)
NGC3675	171.53575	43.58592	10.29	9.42	16.8	2.0	7.38	0.020	0.47	0.0026	Sb	2	0	0	(2)
NGC3726	173.33802	47.02920	10.74	10.11	13.6	2.0	8.39	0.017	0.60	0.0029	Sc	1	0	0	(2)
NGC3941	178.23066	36.98633	10.88	10.19	13.8	0.1	4.90	0.021	0.68	0.0030	S0	1	0	0	(3)
NGC3953	178.45382	52.32677	10.65	9.82	18.8	1.0	8.32	0.030	0.50	0.0035	Sbc	0	0	2	(7)
NGC3972	178.93787	55.32074	12.27	11.60	20.8	0.2	8.27	0.014	0.27	0.0028	SABb	3	0	9	(8)
NGC4010	179.65787	47.26150	12.81	12.09	17.9	2.0	7.80	0.024	0.22	0.0030	SBcd	1	0	0	(2)
NGC4220	184.04880	47.88326	11.78	10.94	20.3	2.0	5.98	0.018	0.33	0.0031	S0-a	3	1	2	(9)
NGC4307	185.52368	9.04363	12.05	11.23	20.0	2.0	7.77	0.023	0.22	0.0035	SBb	5	2	5	(2)
NGC4321	185.72846	15.82182	10.21	9.53	15.2	0.5	8.63	0.026	0.84	0.0053	SABb	4	0	4	(10)
NGC4689	191.93985	13.76281	11.38	10.73	15.0	2.2	6.13	0.023	0.77	0.0054	Sc	2	0	0	(2)+(3)+(4)
NGC5033	198.36444	36.59394	10.68	9.93	19.1	2.0	11.35	0.012	0.44	0.0029	Sc	2	0	0	(9)
NGC5248	204.38343	8.88518	10.89	10.16	14.9	1.3	7.54	0.024	0.67	0.0038	SABb	2	0	0	(11)
NGC5866	226.62291	55.76321	...	...	14.1	0.5	7.89	0.013	0.40	0.0022	S0-a	6	1	2	(12)
NGC5907	228.97404	56.32877	10.50	9.66	16.5	0.1	21.16	0.011	0.11	0.0033	SABc	6	0	2	(3)
NGC6015	237.85512	62.31003	11.16	10.54	19.0	0.2	9.10	0.013	0.48	0.0028	Sc	1	0	0	(3)

Note. Reference codes ($D_{\rm ref}$) correspond to (1) M. Monelli & I. Trujillo (2019); (2) R. B. Tully et al. (2016); (3) E. J. Shaya et al. (2017); (4) E. Kourkchi et al. (2020); (5) O. G. Nasonova et al. (2011); (6) B. A. Jacobs et al. (2009); (7) S. Bose & B. Kumar (2014); (8) A. G. Riess et al. (2016); (9) R. B. Tully et al. (2013); (10) W. L. Freedman et al. (2001); (11) E. Kourkchi & R. B. Tully (2017); and (12) M. Cantiello et al. (2007).

2.2.1. Data Preprocessing and Bias Subtraction

At this initial stage, we work on each CCD of the camera individually. To prepare the data for processing, we create a bad pixel mask that covers the pixels that do not contribute to the signal, due to detector readout failures, and where saturation is leading to a nonlinear detector response. We subtract the overscan, crop the overscan region, construct a master bias image for each CCD, and subtract the corresponding master bias from each image. The master bias is constructed by combining 30 individual bias frames using a sigma clip mean (3σ) algorithm provided in Gnuastro's Arithmetic program (`astarithmetic`).

2.2.2. Flat-field Correction

Precise flat-field correction is crucial for our research. Dome flats are unsuitable for deep imaging, due to irregularities in the LBT dome illumination. Moreover, twilight flats do not fully meet our needs, due to variations between night-sky illumination and the twilight light gradient from the horizon where the Sun has set. To sidestep these issues, we create a master flat using our own set of science images. Although one might suspect that using the complete set of science images would produce a higher-quality master flat, small variations in focus, vignetting, air mass, and moon illumination from night to night, along with light pollution from nearby populations and the scattered light from bright stars, result in less than optimal flat-field frames. To address this problem, we use only data obtained on each night to create the flat-field image for that night's data. We require at least 15 science images each night with which to create the master flat for that specific night. This minimum number is essential for statistical robustness.

For every night of observation, each filter, and each CCD, we generate a distinct master flat using bias-corrected science images. Our process involves two steps. First, we identify those CCD images that we need to reject because the large-scale illumination is grossly nonuniform. Such images deviate from the typical background illumination, potentially introducing erroneous gradients that become noticeable in the final stack. We have a variety of criteria that we impose. We reject CCD images that contain a bright star ($M_V < 9$ mag) or where the target galaxy covers 60% or more of the CCD. We also reject from the stack any CCD images where the distance between the central pixel and a bright star is small (a sliding scale based on the brightness of the star being considered, ranging from $7'$ for a 5.5 mag star to $5'$ for an 8.5 mag star) or where the distance between the central pixel and the target galaxy is equal to or less than half the semimajor axis of the galaxy. The percentage of images excluded per CCD varies depending on the specific field, ranging from 5% to 30% in both g and r filters. By employing dithering with large displacements, we ensure that there are enough frames that are clear of the central galaxy for every CCD. Then, we create the master flat using the procedure described by I. Trujillo et al. (2021). Bias-corrected science images in each filter are divided by their corresponding CCD final flat-field image. To avoid vignetted regions at the corner of the detectors, we remove from the images all pixels where the final flat-field image has an illumination fraction that is < 0.9.

2.2.3. Astrometry, Sky Subtraction, and Photometric Calibration

We determine the astrometry of our individual science images as follows. We initially compute the astrometric solution using Astrometry.net (v0.85; D. Lang et al. 2010) and use Gaia eDR3 (Gaia Collaboration et al. 2021) as our astrometric reference catalog. Because each CCD of the LBC exhibits its own distortions, we employ SExtractor (v.2.25.2; E. Bertin & S. Arnouts 1996) to create object catalogs for each CCD and SCAMP (v.2.10.0; E. Bertin 2006), again using Gaia eDR3 as the reference catalog, to obtain higher-fidelity astrometric solutions. Using the astrometric solutions obtained using SCAMP, we next apply SWarp (E. Bertin et al. 2002) to each individual image to map it to a common coordinate grid.

Proper sky subtraction is key when dealing with low surface brightness data, to avoid introducing artificial gradients and impacting the subtle structures that might be there. We assume that each individual CCD image's sky level can be approximated by a single constant value. We do this to avoid inadvertently modeling out physical low surface brightness features and expect our extensive dithering to mitigate spatial variations in the sky. Gradients due to scattered light from bright stars will be addressed separately using a well-determined point-spread function. To compute the sky, we employ the `--checksky` option in NoiseChisel (M. Akhlaghi 2019). Initially, we mask bright sources and diffuse light because including them will result in a background value that is biased high and result in an oversubtraction of the background. Subsequently, we determine the sky value for each image by calculating the 3σ clipped median of the nonmasked pixels. By working with CCD images covering an area of approximately $14' \times 8'$, we ensure that we obtain a locally representative sky value for that specific region. Subsequently, for each CCD image taken throughout the night of observation, we subtract the corresponding sky value.

After sky subtraction, we convert the LBT counts (ADUs) into nanomaggies.[11] To do this, for each set of images, we construct a catalog of sources in common between the SDSS and LBT images, cross-referencing with Gaia eDR3 to confirm we have point-like sources, and measure fluxes within circular apertures with a diameter of $2''$ (for Gnuastro routines to do this, see S. Eskandarlou et al. 2023). We compute the flux ratios between the SDSS and LBT sources for each CCD separately. We calculate the resistant (3σ rejection) median of these ratios, and multiply the LIGHTS image by this median to obtain the pixel values expressed in units of nanomaggies. When working with images that may exhibit variations in signal, noise, or instrumental effects, performing astrometric and photometric calibration before stacking allows for optimal control. Comparing across images with different image quality and using apertures of different sizes, we conclude that the zero-point uncertainties are in the range of 0.01–0.02 mag.

2.2.4. Image Stacking

We combine individual exposures to create a final mosaic image using a weighted average, because observational conditions change throughout the night. Some of these variations are well understood and to some degree under our control, such as those that depend on the air mass and depend on the position of the target in the sky. However, some are not

[11] see https://www.sdss3.org/dr8/algorithms/magnitudes.php.

Table 2
LIGHTS Target Galaxies: Observational Details

Name	FWHM$_g$[a] (arcsec)	FWHM$_r$[b] (arcsec)	<air mass>	FOV[c] (arcmin)	FOV(70%)[d] (arcmin)	T_{exp} (hr)	$<T_{exp,70}>$ (hr)	$\mu_{lim,g}$[e] (mag arcsec^{-2})	$m_{lim,g}$[f] (mag)	μ_{lim_r} (mag arcsec^{-2})	$m_{lim,r}$ (mag)
NGC 1042	0.99	1.00	1.38	37.0	20.0	1.5	1.27	31.53	27.77	30.69	26.83
NGC 2712	1.03	1.00	1.24	37.7	18.4	1.5	1.29	31.83	28.22	30.85	27.06
NGC 2903	1.19	1.21	1.18	49.1	19.0	1.5	1.17	30.80	26.89	30.26	26.14
NGC 3026	1.30	1.55	1.17	39.2	22.3	1.5	1.34	30.57	26.61	30.00	25.83
NGC 3049	1.09	1.10	1.10	38.4	21.3	1.0	0.85	31.14	27.43	30.45	26.71
NGC 3198	1.37	1.44	1.16	42.4	22.1	1.5	1.33	31.42	27.38	30.65	26.60
NGC 3351	2.05	2.02	1.29	42.3	16.6	1.0	0.84	30.87	26.43	30.18	25.72
NGC 3368	1.12	1.16	1.11	39.4	20.7	1.5	1.34	31.27	27.42	30.40	26.58
NGC 3486	1.60	1.59	1.07	40.2	18.1	1.5	1.21	31.36	27.10	30.54	26.38
NGC 3596	1.30	1.20	1.08	37.8	22.1	1.6	1.43	31.50	26.74	30.84	26.12
NGC 3675	0.91	1.17	1.03	41.9	21.0	1.5	1.33	31.34	27.71	30.64	26.58
NGC 3726	1.10	1.25	1.34	42.0	21.1	1.5	1.32	31.10	27.28	30.69	26.83
NGC 3941	1.00	1.22	1.32	40.7	22.2	1.45	1.30	31.43	27.79	30.75	26.81
NGC 3953	1.23	1.40	1.14	42.2	21.0	1.5	1.32	31.22	27.44	30.69	26.56
NGC 3972	1.05	1.22	1.14	43.9	20.6	1.5	1.21	31.23	27.43	30.60	26.75
NGC 4010	1.99	1.52	1.05	37.5	22.8	0.5	0.42	30.38	25.95	29.88	25.72
NGC 4220	1.85	1.69	1.27	43.9	22.2	1.75	1.58	31.52	27.10	30.96	26.68
NGC 4307	1.17	1.69	1.15	37.5	20.8	2.5	2.23	31.56	27.70	30.92	26.84
NGC 4321	1.14	1.25	1.23	41.5	19.3	2.0	1.74	30.70	26.91	29.93	26.13
NGC 4689	1.61	1.64	1.29	37.7	21.0	1.0	0.85	31.01	26.81	30.39	26.13
NGC 5033	1.15	1.33	1.20	44.8	18.8	1.7	1.48	31.35	27.41	30.56	26.55
NGC 5248	1.05	1.03	1.13	39.1	20.6	1.45	1.29	31.23	27.61	30.60	26.89
NGC 5866	1.14	1.24	1.09	41.7	20.4	3.1	2.77	32.01	28.24	31.20	27.13
NGC 5907	1.19	1.35	1.10	50.2	20.4	1.5	1.28	31.44	27.45	30.80	26.68
NGC 6015	1.24	1.34	1.22	44.7	22.3	1.5	1.34	31.29	27.30	30.70	26.62

Notes.
[a] Measured in the g band using point-like sources in the final image.
[b] Measured in the r band using point-like sources in the final image.
[c] The final FOV is a square with a length of the given value.
[d] The FOV (70%) is the field observed for $T_{exp} > 70\%$. The FOV (70%) is a circle with a diameter of the given value.
[e] Surface brightness limit is computed using the extended metric of 3σ detection in areas equivalent to $10''$ by $10''$ boxes.
[f] Limiting magnitude for point-like sources computed within an FWHM radius circular aperture (5σ detections).

well understood and are beyond our control, such as meteorological events like passing clouds that affect the sky brightness. The latter will generate artificially high standard deviations in the sky pixel values, indicative of poorer image quality. To mitigate these variations, images obtained in better conditions should carry more weight in the final mosaic. Therefore, we use a weighted average to combine the images, with a weight for the ith image equal to the ratio of the standard deviation of the sky in the best exposure to the standard deviation of the sky in the ith image. To compute the standard deviation of the sky in each image, we begin by using the procedure described in Section. 2.2.3 to create a mask for bright sources and diffuse light. We then calculate the 3σ clipped standard deviation of the nonmasked pixels in each image. A complication in calculating the weighted mean is that it is strongly influenced by outliers such as cosmic rays. Cosmic rays typically manifest as isolated pixels with high values (exceeding 3σ from the mean) and are correctly not recognized as sources by NoiseChisel. We identify such pixels as those having a value that deviates from the sigma-clipped mean (3σ rejection is sufficient for our purpose) of all pixels at the same sky location, in all images. We mask these outliers and stack the data using the ``sigclip''—weighted mean routine in gnuastro's Arithmetic program. The co-added image is significantly deeper than any individual image, and therefore, low surface brightness features, previously invisible, emerge from the noise. Therefore, we repeat the sky estimation (and subsequent reduction steps described previously) on the individual images using the improved masks generated by the first data co-add to produce our final data co-add. We provide a detailed quantification of each step of the data reduction pipeline in G. Golini et al. (2024, in preparation) for the specific case of NGC 3486.

We tabulate the observational parameters, final image quality, and limiting magnitudes in Table 2. The quoted limiting magnitude and surface brightness limits correspond to regions within each field that have been observed for more than 70% of the total exposure time. In calculating the surface brightness limits, we apply the mask created from the deeper $g + r$ data. We evaluate the variance in the unmasked pixel values for each image, adopt that as representative of the uncertainty in each pixel, and then calculate the 5σ limit for a circular aperture with a radius equal to that of FWHM of each particular image, to estimate the limiting magnitude and the 3σ limit for an area equivalent to a $10''$ by $10''$ box, to estimate the limiting surface brightness. As such, we assume that each pixel is independent. We find a range of approximately one magnitude in our limits across fields that have the same exposure time. We have traced some of this variation to differences in seeing conditions, air mass, scattered light, light pollution, and proximity to the moon and its illumination. The moon has the clearest effect in the magnitude limit, although a

Table 3
Number of Detections and LSB Satellite Galaxy Candidates in LIGHTS versus Processing Step[a]

Process	Step in Section 3	Detections[b]	LSB Candidates[b]
Wavelet screening	3	717,124 (28,685; 20,038 to 55,374)	NA
Object matching	4	541,086 (21,643; 14,140 to 49,328)[c]	261,046 (10,442; 7036 to 20,330)
Sérsic screening	5	211,104 (8,444; 5,114 to 14,215)	153,552 (6,142; 3864 to 10,733)
Initial GALFIT screening	6	NA	27,209 (1088; 686 to 1822)
Final GALFIT screening	7	NA	6044 (241; 157 to 394)[d]
Visual Examination	8	NA	62 (2.48; 1 to 9)

Notes.
[a] Entries may include detections or candidates that are common to the two runs.
[b] Values in parentheses denote the mean number of detections per field and the range in that value among the target galaxies.
[c] Includes duplicates.
[d] Duplicates deleted.

large fraction of the total variation in the limiting magnitude remains unaccounted for and presumably reflects variations in the atmospheric properties at the time of observation.

3. Our LSB Satellite Search

We base our pipeline for identifying LSB satellite galaxy candidates on that used for our processing of the Legacy Survey (D. Zaritsky et al. 2023), but major modifications are required for LIGHTS because of its much greater depth, larger file sizes, and the availability of only the g and r bands (the Legacy Survey also has z-band observations; A. Dey et al. 2019). The major steps for identifying potential LSB satellites in LIGHTS are (1) image processing that produces a preliminary list of candidates, (2) visual confirmation of remaining candidates, (3) estimation of completeness using simulated sources, and (4) creation of the catalog.

This procedure is a significant departure from D. Zaritsky et al. (2023), where we also rejected candidates based on thresholds for cirrus contamination and screened survivors with a machine-learning classifier before visual confirmation. These steps are unnecessary in LIGHTS because target galaxies were already selected in regions of low extinction, and its relatively small total footprint, as opposed to the $\sim$20,000 deg^2 of the Legacy Survey, allows for visual confirmation of all candidates.

Details of the Legacy Survey pipeline have been previously described, and other than brief summaries, we only address modifications here. Because of the reasons noted in Section 3, Step 3, we make two passes through the pipeline and the number of potential candidates surviving each step discussed below represents the final total after the two runs. Processing and analysis of calibrated LIGHTS images is performed using the facilities of the University of Arizona High Performance Computing center.[12]

We identify potential LSB satellite galaxy candidates using the following steps, and summarize these in Table 3:

1. Because of the large size of the LIGHTS mosaics, we start by binning them by a factor of four in each direction, which also increases the signal-to-noise ratio. While this increases the pixel scale from $0\farcs224$ pixel^{-1} to $0\farcs896$ pixel^{-1}, the effective pixel size is still significantly smaller than our minimum allowable candidate satellite size (3.5 rebinned pixels or $r_e = 3\farcs2$, which we find to be a coarse lower size limit on the resolution needed for reliable model fitting and classification). The LIGHTS pipeline flags saturated regions, bad pixels, and image regions outside of the observation area with NaN values. We replace these NaN values using the Python ASTROPY interpolate_replace_nans function.
2. To limit the number of candidates requiring further processing in the Legacy Survey, D. Zaritsky et al. (2023) subtracted sources that were clearly too bright to be their intended targets. This step required masking out to the periphery of these bright objects. However, the significantly greater depth of the LIGHTS images results in a much higher density of such objects, and we skip this step to avoid excessive masking.
3. As described in detail by D. Zaritsky et al. (2019), the detection pipeline uses wavelet transforms with tailored filters to isolate candidates of different angular scales. Higher wavelet levels will preferentially accentuate objects of larger sizes. However, clusters of small objects can be detected across multiple wavelet levels. To limit the number of false detections when processing Legacy Survey images, D. Zaritsky et al. (2023) required that higher-order wavelets have a peak value of at least 25% of lower-order wavelets within its footprint. Because of the greater depth in LIGHTS, and the resulting larger number of overlying contaminants, we found that we initially missed some obvious LSB candidates when using this criterion, and therefore we chose to repeat our processing without this requirement. With this change, we find a total of 717,124 wavelet detections.
4. We limit spurious detections by requiring that a potential candidate have coincident detections in both filter bands (defined as center-to-center separations $< 4''$), with its resulting location defined as the midpoint of the two centers. This criterion results in the acceptance of 541,086 wavelet detections which are, after eliminating nearby duplicates (defined to be other detections within $4''$), associated with 261,046 groups of detections needing further processing.
5. The vast majority of detections surviving the previous steps are still not viable LSB satellite galaxy candidates and require further filtering. Rather than using time-consuming GALFIT modeling (C. Y. Peng et al. 2002) at this point, we obtain rough parameter estimates by fitting an exponential Sérsic model ($n = 1$) with the much faster LEASTSQ function from the Python SciPy library (E. Jones et al. 2001). Because this modeling is only used as a coarse selection screen, we require that results

[12] https://public.confluence.arizona.edu/display/UAHPC/Resources

meet conservative parameter thresholds of $r_e \geqslant 2\farcs7$ and $\mu_0 \geqslant 23.0$ and 22.0 mag arcsec^{-2} for the g and r bands, respectively, to avoid prematurely rejecting good candidates. An important clarification, in particular with respect to our discussion of nucleated sources in Section 6.2, is that we mask bright regions in the center of each candidate when fitting models (see D. Zaritsky et al. 2023, for details). Despite this initial use of a fixed n, final samples from this procedure show no bias against higher-n objects at least up to $n = 2$ (D. Zaritsky et al. 2021). A total of 211,104 detections comprising 153,552 distinct candidates survive this step.

6. We now revisit the modeling using the combination of the g- and r-band images to reach greater depth, a slightly refined model, and additional selection criteria. We now do use GALFIT to model each candidate using a fixed Sérsic index, $n = 1$, and again use generous acceptance thresholds of $r_e \geqslant 2\farcs7$, $b/a \geqslant 0.34$, and $\mu_{0,g} \geqslant 23$ mag arcsec^{-2}, or $\mu_{0,r} \geqslant 22.2$ mag arcsec^{-2} if there is no available measurement of $\mu_{0,g}$. Once again, the values are set to avoid prematurely rejecting acceptable candidates. A total of 27,209 candidates meet these criteria.
7. In our final image processing step, we model the remaining candidates using GALFIT with a variable Sérsic index and an estimate of the PSF derived from the FWHM parameter given in Table 2 for both g- and r-band images. To avoid having a nuclear star cluster distort the fit, we mask the center if those pixels are a factor of two brighter than our central surface brightness limits (24 and 23.6 mag arcsec^{-2} for g and r, respectively). After applying our final, tighter LSB candidate criteria of $r_e \geqslant 3\farcs2$, $\mu_{0,g} \geqslant 24$ mag arcsec^{-2} (or $\mu_{0,r} \geqslant 23$ magarcsec^{-2} if GALFIT failed to model the g-band image), $b/a \geqslant 0.37$, and $n < 2$, we are left with a total of 6044 candidates requiring further evaluation. These parameter choices mirror those in D. Zaritsky et al. (2023) and are discussed in more detail there.
8. The remaining candidates are visually reviewed by D.Z. and R.D., with each candidate labeled as a potential LSB satellite or a false positive. Those with disagreements are classified again by both reviewers. This procedure results in both reviewers labeling 62 as LSB candidates, with the remainder classified as a false positive by at least one of the reviewers. To minimize the number of false candidates in our final list, we consider any disagreements between the two reviewers to be false positive (five objects are in this category).

Visual classification—in fact, any type of morphological classification—has the potential to introduce unintended biases in the properties of the final sample. We attempt to reject only objects that are evidently not galaxies (e.g., tidal tails, merged groups of background galaxies, and image artifacts), but biases could nevertheless creep in. In our comparison of the SMUDGes catalog with other catalogs (D. Zaritsky et al. 2021, 2023) and our comparison here to independent work (Section 5), we do not identify any significant classification disagreements among galaxies in common that satisfy the stated selection criteria of either survey, suggesting that we are not introducing any peculiar biases with our visual classification, although it is possible that all surveys share similar biases.

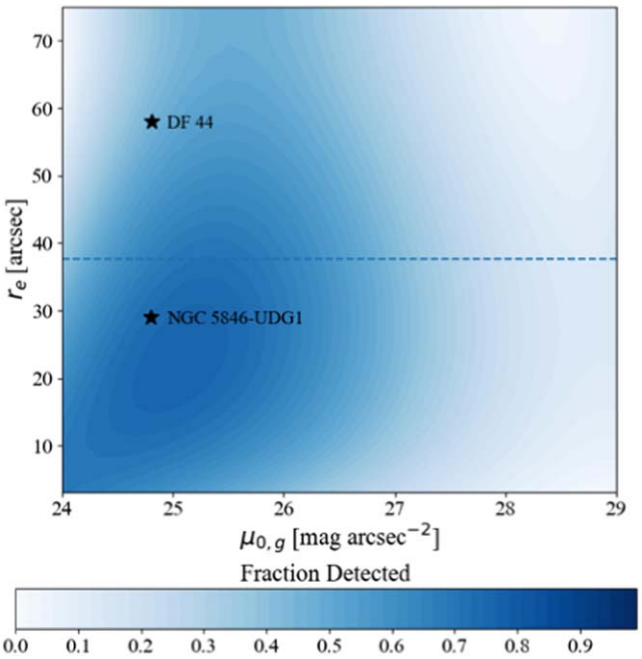

Figure 2. Recovered completeness as a function of g-band central surface brightness and angular size on average across the survey. For guidance, we plot the locations of two well-known UDGs, DF 44 and NGC 5846-UDG1, if they are placed at the median LIGHTS distance (15.2 Mpc). The photometric data for DF 44 comes from D. Zaritsky et al. (2023), while that for NGC 5846-UDG1 comes from D. A. Forbes et al. (2019). We also show the upper end of the r_e range of the galaxies we have found with the dashed line. We are highly complete in such systems to a central surface brightness approaching ~27 mag arcsec^{-2}. We note, however, that the lowest surface brightness Milky Way satellite known, Antlia 2 (G. Torrealba et al. 2019), lies at $\mu_{0,g} = 30$ mag arcsec^{-2}, assuming $V - g = -0.3$ and $\mu_0 = \mu_e - 1$ (A. P. Ji et al. 2021), and is well beyond our capability to detect with this survey.

3.1. Estimating Completeness

We define completeness as the probability that a candidate with given structural and photometric parameters survives our pipeline. We estimate that probability by placing simulated LSB satellites with Sérsic profiles and random structural and photometric properties within the image and processing them separately with the same pipeline that was used for our real sources. These are placed in a fixed grid with nodes separated by 80″ in each direction, resulting in a simulation density of 2025 deg^{-2}. Because we are primarily interested in the impact of $\mu_{0,g}$ and r_e on completeness, we fix the other parameters ($g - r$ color, b/a, n) to their respective median values for the science candidates (0.61 mag, 0.68, and 0.81). We sample the parameter ranges of $23 \leqslant \mu_{0,g} < 29$ mag arcsec^{-2} and $2.7 \leqslant r_e < 23''$. These limits are set to optimize coverage of the parameter range sampled by our candidates. We then extend the range of our completeness simulations to $r_e = 70''$, at lower sampling density than what is described immediately below, to broadly explore our overall detection sensitivity (Figure 2). These values are representative across the full survey. There are fields, and areas within fields with more overlapping exposures, where we go deeper than indicated by these representative values.

To obtain enough data to adequately model completeness, we run the simulation routine 20 times, which produces 339,625 simulations that fall within the image boundaries. Those sources where >30% of the pixels within one r_e have

NaN values are ignored. We consider any candidate surviving the entire pipeline and lying within 4″ of a simulated source to be a potential detection of that simulated source. However, such candidates may also result from the detection of a real source in that same area. We account for such superpositions by deleting any simulation that lies within 4″ of a candidate produced by the science pipeline before visual confirmation, leaving us with 338,459 simulated sources, of which 189,670 (56%) survive the pipeline.

We use these results to derive the completeness as a function of $\mu_{0,g}$ and r_e using a second-degree polynomial model. To derive that model, we use the PolynomialFeatures function from the Python Scikit-learn library (F. Pedregosa et al. 2011) and a three-layer neural network implemented with Keras (F. Chollet & Keras Team 2015). For the interested reader, details on how the parameter window size and the degree of the polynomial model are selected are described in D. Zaritsky et al. (2021). This procedure provides a good fit to the simulation results with a Coefficient of Determination, R^2, of 0.98. The resulting model (Figure 2) is then applied to the particular parameters of each science candidate, to assign each its own individual completeness estimate f_C. Those values are presented in Table 4. For three LSB candidates, we either do not have the necessary data or they fall outside of the parameter space defined by the model. These are designated with $f_C = -1$ in the table, but we adopt the mean completeness (0.56) for these three candidates when generating figures where we apply completeness corrections.

4. Results

We identify 62 low surface brightness ($\mu_{0,g} > 24$ mag arcsec^{-2}) candidate satellites around 25 target galaxies (Table 1). We reject eight of these that, upon further review, we consider to be background objects (Figure 3). In some cases, these appear to have spiral structures, and are therefore likely to be background disk galaxies. In others, they are comprised of a set of small, distinct sources that are likely to be distant galaxy groups or clusters (e.g., A. H. Gonzalez et al. 2001). These are among the smallest, highest surface brightness galaxies in our sample, which is the parameter range where one would expect to find background objects. We present the remaining 54 candidate satellites in Figure 4 and Table 4. Uncertainties are not included, because the internally estimated errors are underestimates. Improved estimates can be obtained from simulations (as done in D. Zaritsky et al. 2023), but uncertainties in the physical parameters, which are of primary interest here, are dominated by distance uncertainties, which are given in Table 1.

The number of low surface brightness satellites candidates per parent galaxy (Table 1) varies between seven and seven, and is reasonably reproduced by a Poisson distribution with mean 2.2 (54/25) that integrates up to 25 systems (Figure 5). The sample size is small, however, and there is a hint that there are more than the expected number of systems with $\geqslant 5$ satellites. Perhaps these systems are not a population of bound satellite galaxies, but rather belong either to a clustered background population or to a rich local environment, if the associated parent galaxies are themselves members of a group. In two cases (NGC 1042 and NGC 4307), the larger $N_{\rm LSB}$ is matched with a large $N_{\rm LEDA}$, suggesting that these are indeed found within group environments. Removing these systems from consideration, we find that the mean number of LSB satellite candidates per parent drops to 1.8 (42/23).

A closer inspection of the numbers, however, must include consideration that our sample spans a range of distances, host galaxy stellar masses, and environments. We expect the first to affect the radial range over which we identify satellite candidates and the physical size distribution of the candidates, and the second, assuming a connection between stellar mass and total mass, to be reflected in the numbers of satellites. The third we have attempted to mitigate by not considering targets in dense environments.

The FOV of the nearest target with the smallest FOV (NGC 3351, $D = 10$ Mpc, and FOV $= 42.'7$ on a side), results in a maximum radius to which we are potentially complete in our satellite search of 62 kpc. Therefore, to compare the numbers of candidate satellites among galaxies fairly, we can either limit all fields to this radius or correct for the incomplete sampling for some targets at larger radii. Considering only the candidates found at $R_{\rm proj} < 60$ kpc, we do find a correlation between the host galaxy magnitude and the number of satellite candidates in the expected sense, but the statistical significance is at roughly only the 1σ level. The average number of satellite candidates within 60 kpc per host in our catalog is 0.84.

Alternatively, we can probe out to a larger $R_{\rm proj}$ and correct for those fields that do not reach these radii. In this approach, we select a radius that many of our fields reach, 100 kpc, and then simply weight the results at the larger radii by the inverse of the fraction of images that sample to that radius.[13] We refer to this as the radial completeness correction, to differentiate it from the photometric completeness one discussed in Section 3.1. When we apply both the radial and photometric corrections, we find that each host galaxy has four satellite candidates out to 100 kpc. Without applying the radial correction, we find that each host has 3.6 candidates to this projected radius. The modest change in numbers after we apply the radial completeness correction reflects that situation that most of our fields do sample out to $R_{\rm proj} = 100$ kpc.

Certain properties of the satellites themselves are provided in Figure 6. In the upper panel, we present the radial distribution of satellites after applying both the photometric and radial completeness corrections. For intuition, note that, if the 3D density of satellites was proportional to r^{-2} (as it would be for isothermal sphere distribution), then the number of satellites per radial bin would remain constant. We find no signs of a significant trend with radius (at $R_{\rm proj} > 100$ kpc, the results are highly uncertain because only a few of our images sample that radial range).

In the middle panel, we present the central surface brightness distribution, which slightly favors brighter central surface brightnesses among the detected candidates, but extends to $\mu_{0,g} \sim 28$ mag arcsec^{-2}. With the photometric completeness correction applied, we find a nearly flat distribution in central surface brightness, with, at most, an allowed increase in numbers of roughly a factor of two from our bright central surface brightness limit to our faint one. We conclude that there is no vast reservoir of such undiscovered galaxies down to at least $\mu_{0,g} \sim 28$ mag arcsec^{-2}.

Finally, the third panel in Figure 6 shows that the distribution in luminosity for these low surface brightness candidate satellites is nearly constant between $-13 < M_r/{\rm mag} < -9$ for

[13] This correction does not address the loss of physically smaller, lower-luminosity satellites of hosts at larger distance, due to our angular size cut. Correcting for this effect requires knowledge of the satellite size and luminosity functions that we do not have.

Table 4
LIGHTS Low Surface Brightness Satellite Catalog

SMDG Designation	Parent	R.A. (°)	Decl. (°)	n	r_e (″)	b/a	PA (°)	$\mu_{0,g}$ (mag/(″)^2)	$\mu_{0,r}$ (mag/(″)^2)	$r_{e,\mathrm{phys}}$ (kpc)	R_{proj} (kpc)	f_C
SMDG0239526-081243	NGC1042	39.96930	−8.21195	0.85	8.70	0.9	−85.1	27.1	26.4	0.57	60.4	0.35
SMDG0240045-082646	NGC1042	40.01880	−8.44614	0.59	16.70	0.7	−15.2	26.8	26.1	1.09	19.1	0.46
SMDG0240069-081343	NGC1042	40.02886	−8.22864	0.94	12.53	1.0	66.0	24.1	23.3	0.82	51.0	0.72
SMDG0240287-081434	NGC1042	40.11961	−8.24291	0.88	11.42	1.0	−44.6	26.5	25.8	0.75	45.2	0.49
SMDG0240406-082308	NGC1042	40.16902	−8.38542	0.36[a]	4.49	0.6	88.3	27.3	26.7	0.29	19.7	0.16
SMDG0240557-082639	NGC1042	40.23225	−8.44416	1.09	5.87	0.8	−42.6	27.9	27.4	0.38	31.0	0.13
SMDG0241094-081749	NGC1042	40.28910	−8.29681	0.62	8.64	0.7	23.9	25.4	24.5	0.57	54.6	0.69
SMDG0858542+443744	NGC2712	134.72591	44.62899	0.84	8.83	0.8	−5.1	25.0	24.5	1.29	160.5	0.75
SMDG0900028+445524	NGC2712	135.01159	44.92331	1.63	4.70	0.8	−27.8	25.7	25.2	0.69	50.5	0.49
SMDG1046186+115918	NGC3368	161.57760	11.98846	1.34	3.36	0.6	−84.1	24.1	23.5	0.18	39.4	0.70
SMDG1046302+114522	NGC3368	161.62565	11.75619	0.51	9.30	0.9	18.2	25.1	24.5	0.51	17.6	0.75
SMDG1047059+115243	NGC3368	161.77454	11.87855	0.52	7.65	0.7	−82.0	26.8	26.2	0.42	19.7	0.38
SMDG1047405+120258	NGC3368	161.91868	12.04932	0.97	10.62	1.0	−84.3	25.8	25.0	0.58	62.6	0.62
SMDG1101447+285507	NGC3486	165.43630	28.91870	0.70	5.57	0.9	51.5	24.7	24.1	0.37	71.2	0.74
SMDG1115343+143132	NGC3596	168.89298	14.52549	1.21	5.58	0.7	49.4	24.1	25.0	0.31	56.2	0.67
SMDG1126214+434408	NGC3675	171.58937	43.73553	1.06	9.52	0.5	87.1	24.0	23.3	0.78	45.3	0.66
SMDG1126532+432749	NGC3675	171.72158	43.46373	0.76	4.90	0.8	−28.4	26.3	25.7	0.40	53.3	0.39
SMDG1132312+470704	NGC3726	173.12985	47.11774	0.98	6.67	0.8	−56.5	27.0	...	0.44	39.7	0.32
SMDG1152340+370702	NGC3941	178.14169	37.11711	0.61	9.32	0.7	−35.1	25.7	24.9	0.62	35.8	0.64
SMDG1155345+551658	NGC3972	178.89382	55.28269	0.82	4.15	0.8	−38.7	27.2	26.6	0.42	16.5	0.18
SMDG1155406+552155	NGC3972	178.91909	55.36520	0.87	11.96	0.4	−47.0	25.8	25.2	1.21	16.6	0.63
SMDG1156093+551556	NGC3972	179.03881	55.26550	0.71	7.54	0.5	66.0	24.4	23.8	0.76	28.9	0.68
SMDG1158469+473107	NGC4010	179.69539	47.51862	0.85	6.20	0.7	−23.7	24.0	23.5	0.54	80.7	0.64
SMDG1214528+474319	NGC4220	183.72000	47.72185	1.12	6.66	0.5	38.0	25.3	24.7	0.66	96.9	0.66
SMDG1215038+473833	NGC4220	183.76590	47.64263	1.25	20.31	0.6	−87.4	26.8	26.5	2.00	108.7	0.45
SMDG1217358+474748	NGC4220	184.39904	47.79678	0.52	3.37	0.8	20.9	26.0	25.7	0.33	88.7	0.34
SMDG1220588+085156	NGC4307	185.24491	8.86568	1.01	14.30	0.5	1.3	24.9	24.1	1.39	114.4	0.72
SMDG1222096+153910	NGC4321	185.53988	15.65282	0.74	15.12	0.8	−15.0	26.1	25.4	1.11	65.8	0.59
SMDG1222266+084719	NGC4307	185.61079	8.78870	0.71	15.57	0.8	−75.4	24.2	24.1	1.51	93.9	0.76
SMDG1222421+085000	NGC4307	185.67536	8.83311	0.56	15.03	0.7	−59.5	24.6	24.1	1.46	90.2	0.74
SMDG1222509+085408	NGC4307	185.71224	8.90232	0.83	11.97	0.5	−14.8	24.6	24.1	1.16	81.6	0.69
SMDG1222512+085046	NGC4307	185.71333	8.84620	0.68	8.27	0.9	−66.3	27.1	26.8	0.80	95.0	0.33
SMDG1222537+160000	NGC4321	185.72376	16.00001	1.19	5.07	0.7	−49.4	24.6	24.1	0.37	47.3	0.75
SMDG1222554+153335	NGC4321	185.73087	15.55973	0.69	10.07	0.8	12.8	25.1	24.3	0.74	69.6	0.74
SMDG1223051+155555	NGC4321	185.77118	15.93186	0.76	12.63	0.5	75.2	24.0	23.3	0.93	31.2	0.72
SMDG1248031+134329	NGC4689	192.01308	13.72468	0.67	17.31	0.6	−28.1	24.2	23.6	1.26	21.1	0.78
SMDG1248294+134819	NGC4689	192.12234	13.80532	0.85	7.56	0.6	−34.7	24.5	23.9	0.55	47.7	0.69
SMDG1314090+362001	NGC5033	198.53739	36.33372	1.03	9.71	0.8	−29.4	26.3	25.5	0.90	98.4	0.52
SMDG1314205+363412	NGC5033	198.58532	36.56995	0.74	15.58	0.6	18.9	...	23.2	1.44	59.7	−1.00
SMDG1337327+090817	NGC5248	204.38635	9.13815	0.78	8.01	0.9	1.6	24.8	24.1	0.58	65.7	0.73
SMDG1337528+085709	NGC5248	204.46989	8.95253	0.63	5.37	0.9	47.0	26.8	26.1	0.39	28.2	0.31
SMDG1504281+554100	NGC5866	226.11690	55.68306	0.74	3.64	0.4	−5.0	25.9	25.3	0.25	72.9	0.38
SMDG1504500+553844	NGC5866	226.20822	55.64542	1.09	11.74	0.9	−84.7	24.1	...	0.80	64.4	0.70
SMDG1505300+555200	NGC5866	226.37487	55.86672	0.79	37.73	0.5	63.7	25.6	...	2.58	42.7	−1.00
SMDG1505523+553200	NGC5866	226.46812	55.53341	0.92	5.89	0.6	66.2	26.1	25.4	0.40	60.5	0.48
SMDG1507165+552829	NGC5866	226.81866	55.47484	0.67	6.24	0.5	−46.0	24.6	24.1	0.43	76.0	0.74
SMDG1508054+555216	NGC5866	227.02246	55.87100	0.35[a]	4.52	1.0	89.7	27.9	27.4	0.31	61.3	0.10
SMDG1514241+562934	NGC5907	228.60050	56.49267	1.01	3.77	0.7	30.8	25.2	24.7	0.30	76.0	0.55
SMDG1514553+561124	NGC5907	228.73041	56.19002	0.90	4.31	0.5	−65.5	...	23.1	0.34	55.8	−1.00
SMDG1515425+564216	NGC5907	228.92694	56.70454	0.30[a]	3.59	0.5	−16.3	27.6	25.9	0.29	108.5	0.12
SMDG1515436+561925	NGC5907	228.93171	56.32362	0.38[a]	6.26	0.5	−31.4	24.2	23.4	0.50	6.9	0.68
SMDG1516240+562637	NGC5907	229.09993	56.44363	0.81	5.85	0.9	−10.7	24.6	24.0	0.47	38.7	0.73
SMDG1516500+561315	NGC5907	229.20851	56.22097	0.66	3.49	0.6	−43.0	25.3	24.8	0.28	48.7	0.51
SMDG1551357+621734	NGC6015	237.89891	62.29272	0.83	15.61	0.8	−41.1	24.6	24.2	1.44	8.9	0.74

Note.
[a] Sérsic index values below 0.5 are not physically meaningful, as they would imply a hole in the center of the object in 3D.

the detected sources. Again, the situation changes slightly after applying the photometric completeness corrections, suggesting a moderate rise in the numbers of smaller, fainter LSB satellites across the parameter range explored here.

In summary, after applying photometric and radial completeness corrections and removing the two systems that we suspect of being contaminated with group members, we find an average of four LSB satellites ($24 < \mu_{0,g}/\mathrm{mag\ arcsec}^{-2} < 28$

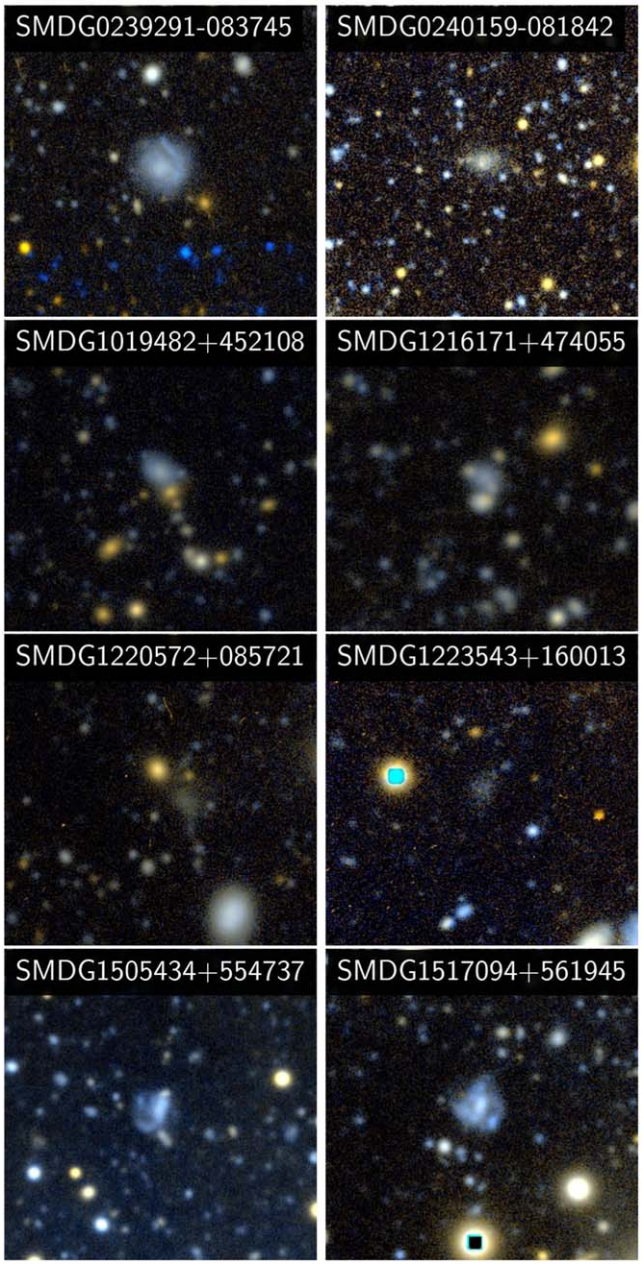

Figure 3. The eight candidates that we reject as background galaxies on the basis of visual appearance, although a few (SMDG0240159-081842, SMDG1220572+085721, and SMDG1223543+160013) might indeed be satellites. The images are ∼70″ on a side and north is up.

and $3.2 < r_e/\mathrm{arcsec} < 23$) per target galaxy out to a projected radius of 100 kpc, and we conclude that the number of satellites at lower levels of luminosity and surface brightness is likely to be larger still, but only by a moderate amount.

5. Comparison with Previous Studies

5.1. SMUDGes

In Figure 7, we present the comparison of our sample cross-matched to the SMUDGes catalog (D. Zaritsky et al. 2023). Focusing on the leftmost two panels among the top set of panels in the figure, which are directly tied to observables used in the selection, we find that there are two clear regimes where our current sample includes galaxies not in the SMUDGes set. These include those with an r_e in angular units that is smaller than the limit adopted by SMUDGes (5.″3) and those with $\mu_{0,g} > 26$ mag arcsec^{-2}. While the former simply reflects the selection criteria of SMUDGes, the latter reflects the shallower effective surface brightness limit of the Legacy Survey data. Completeness simulations carried out for SMUDGes (presented in Figure 9 of D. Zaritsky et al. 2021) clearly show the completeness decreasing quickly at $\mu_{0,g} \sim 26$ mag arcsec^{-2}. As such, data as deep as those in LIGHTS will complement the Legacy Survey data by revealing compact low surface brightness galaxies and galaxies that have central surface brightness up to ∼2 mag fainter than the faintest in SMUDGes.

Within the regime where we expect SMUDGes to find galaxies ($r_e \geqslant 5.''3$ and $24 < \mu_{0,g}/\mathrm{mag\ arcsec}^{-2} < 26$), we find that LIGHTS finds 80% more galaxies (25 versus 14). This is in broad quantitative agreement with the relative overall completeness levels of the LIGHTS survey over this parameter range (69%) and that for SMUDGes (48%; D. Zaritsky et al. 2023).

The rightmost panels in Figure 7 show how the catalog is mostly limited to $R_{\mathrm{proj}} < 100$ kpc, as already discussed.

5.2. ELVES and KMTNet

Two recent surveys targeting faint satellites of nearby galaxies in intermediate to low-density environments are those of S. G. Carlsten et al. (2022; the ELVES survey), based on CFHT imaging complemented with Legacy Survey data, and H. S. Park et al. (2017, 2019), based on imaging results from the KMTNet SNe survey. T. J. Fan et al. (2023) presented a comparison of those two sets of data, and we reprise that comparison including our LIGHTS detections in Figure 8. To make this comparison, we assume $g - V = 0$, which is likely to be off by less than 0.2 mag for blue galaxies (M. Fukugita et al. 1995), but could be off by ∼0.5 mag for redder systems. Even so, neither of these differences is large enough to invalidate the qualitative comparison discussed here.

Our sample is consistent with those two samples once our imposed central surface brightness cut is accounted for. Our catalog extends to lower-luminosity systems, by one or two mag, in at least some of our fields. Even when the depth is comparable, ELVES is limited to galaxies with distances < 12 Mpc, while the LIGHTS sample only has 4 out of 25 within 12 Mpc. A nearby sample has some advantages, such as the possibility that distances can be measured using surface brightness fluctuations, but a more distant grasp provides a much larger potential sample as large-area, deep imaging becomes more available.

We share one parent galaxy in common with the ELVES sample, NGC 2903. We detect zero LSB dwarfs in our images, while Carlsten et al. (2022) list seven satellites. Of those, however, all but two have central surface brightness significantly larger than our cut at 24 mag arcsec^{-2}, and the remaining two are outside of our field of view. We therefore do not find evidence of a discrepancy despite the initial impression.

5.3. SDSS

We do not anticipate much overlap with SDSS, given our surface brightness criterion, but the potential for serendipitous spectroscopic information is of interest. Three of our galaxies (SMDG0240069-081343, SMDG0240287-081434, and SMDG1101447+285507) match three SDSS galaxies

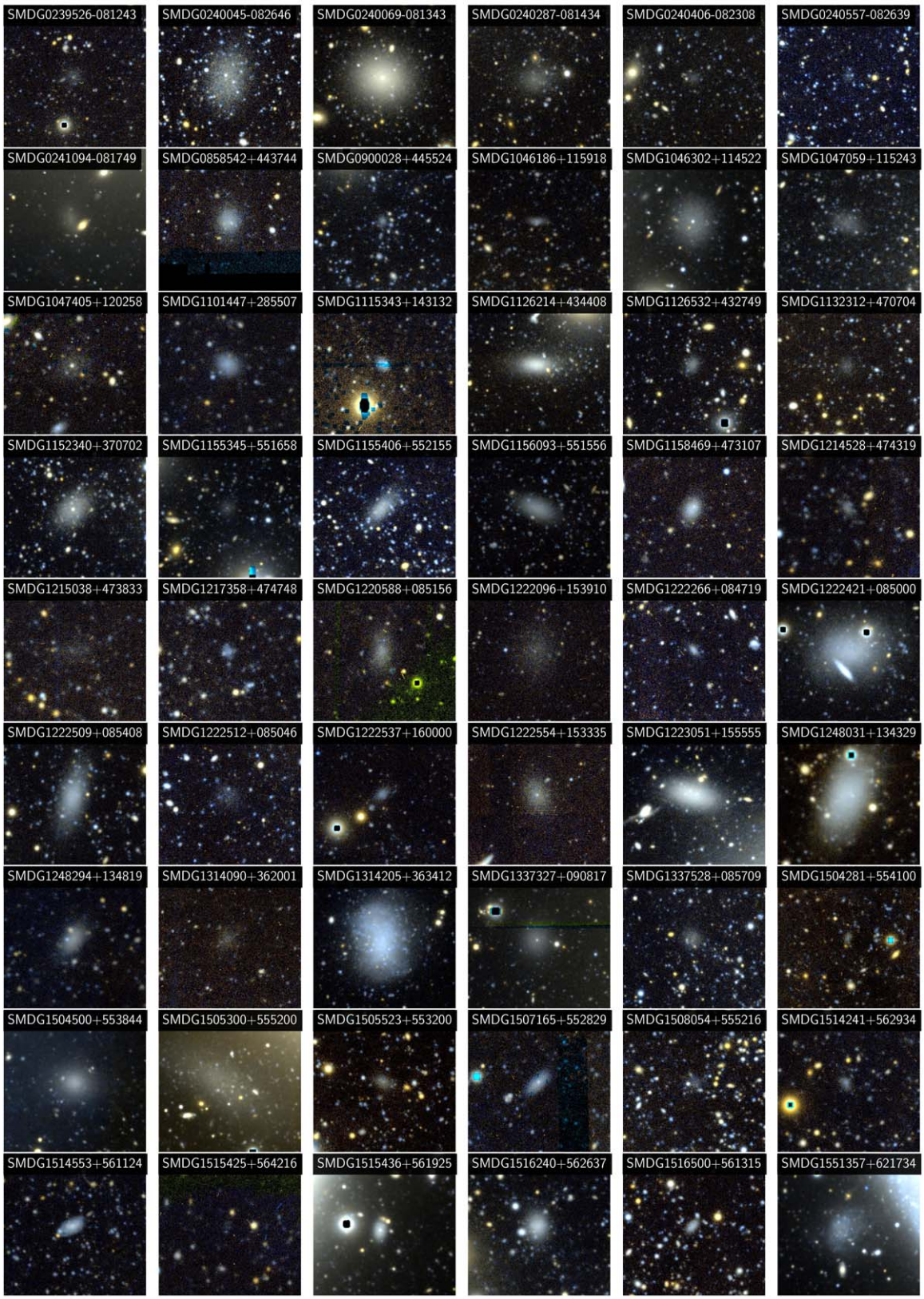

Figure 4. Low surface brightness candidate satellite galaxies identified around LIGHTS galaxies (Table 4). Each panel is $\sim 1\farcm5$ on a side, with north at the top. The color images are created by combining the *g* and *r* bands using `astscript-color-faint-gray` (R. Infante-Sainz & M. Akhlaghi 2024).

(SDSS J024007.01-081344.3, SDSS J024028.61-081436.7, and SDSS J110144.69+285508.2 respectively) to within $2''$. The first and last of these have associated redshift measurements in the SIMBAD database (0.9332 and 0.80471, respectively). Unfortunately, these redshift values are both implausible for these two objects, which have large

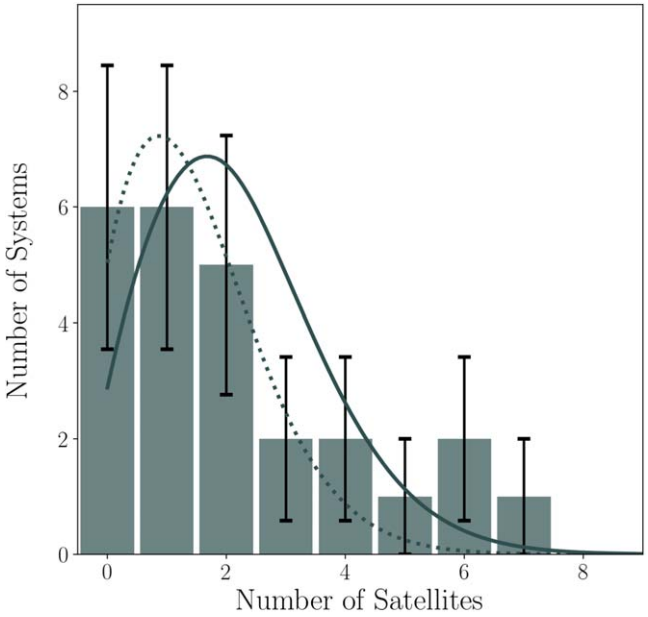

Figure 5. The distribution of target galaxies as a function of low surface brightness satellite count (not corrected for completeness). Solid line is a Poisson distribution with mean 54/25 that integrates to 25 systems. The error bars represent $\sqrt{N}$ uncertainties only. The dotted line revisits the Poisson fit if we exclude systems with >5 satellites. The mean in this case is 1.4 LSB identified satellite candidates per host.

angular extent and low surface brightness. Of these, the first is likely an erroneous SDSS measurement (it comes with a warning in the SDSS database and its spectrum has a signal-to-noise ratio of 3.9) and the second reflects the redshift of a more distant object, a galaxy cluster, seen in projection (T. Szabo et al. 2011).

5.4. MATLAS

The MATLAS survey provides perhaps the most comparable data for comparison, although they obtain deep imaging primarily for elliptical galaxies (P.-A. Duc et al. 2015; M. Bílek et al. 2020). Nevertheless, there is some overlap in target samples, and M. Poulain et al. (2021) provide photometric properties for the dwarf galaxies identified using MATLAS. A general comparison between the MATLAS sample and ours is presented in Figure 8.

We present in Table 5 the associations of 10 of our galaxies with objects in the MATLAS survey. These are satellites around either NGC 3368 (designated as satellites of NGC 3379 in MATLAS), NGC 3941, NGC 3972 (designated as satellites of NGC 3998 in MATLAS), or NGC 5866. The MATLAS catalog contains many more sources in the vicinity of the common targets, but after eliminating galaxies at projected radii > 100 kpc, where we are mostly incomplete, and galaxies with $\mu_{0,g} < 24$ mag arcsec^{-2}, we find only an additional five sources that are not in our catalog (MATLAS-734, MATLAS-756, MATLAS-1122, MATLAS-2053, and MATLAS-2083). MATLAS-734 was rejected because our visual inspection resulted in one reviewer rejecting it. Recall that, in the case of a disagreement, we opted to reject the detection. MATLAS-756 is beyond the edge of our image. MATLAS-1122 was rejected because our fitting latched onto a nearby star and it failed our structural parameter selection criteria. MATLAS-2053 failed the Sérsic n criterion. MATLAS-2083 failed to produce an acceptable model at all. Errors as seen in the last three objects, due presumably to nearby contaminating objects, will be captured by our completeness simulations. These three objects all appear visually to be valid satellites candidates, and therefore we conclude that we found 10 of 13 satellite candidates that match our search criteria (77%), which is a fraction entirely consistent with our estimated completeness. Note that in only one case was our visual classification the likely cause of the disagreement.

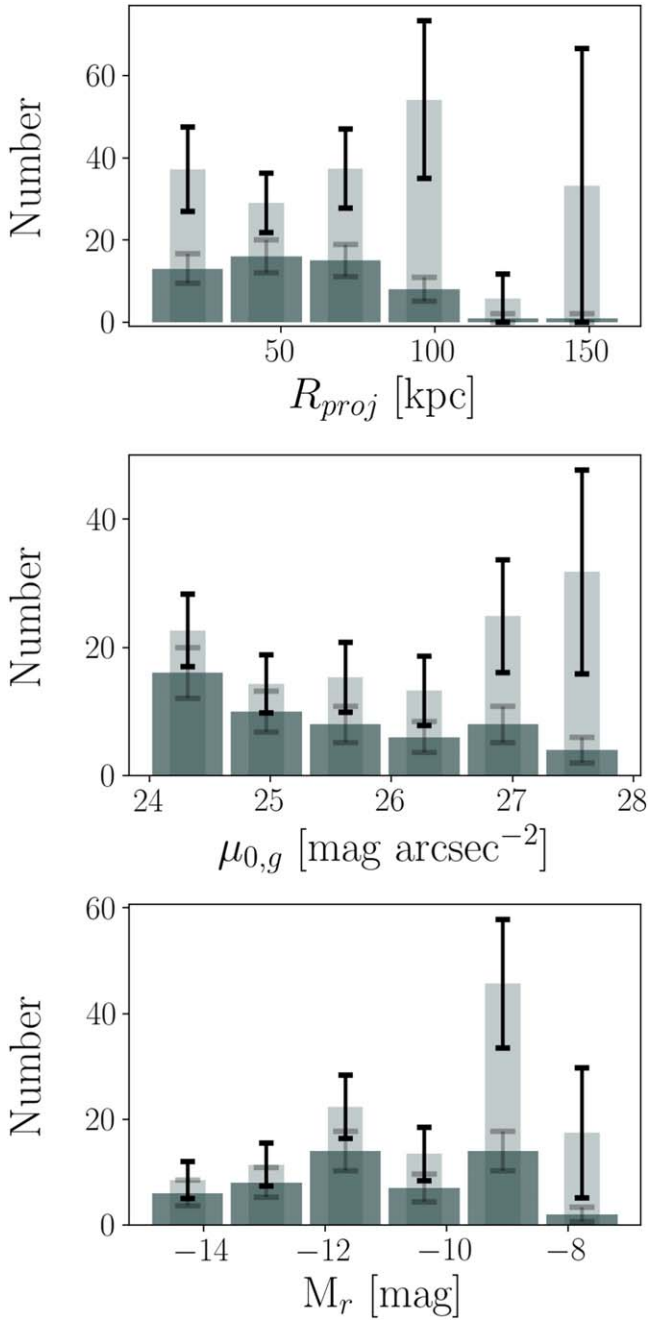

Figure 6. Basic properties of the satellite sample. Histograms represent objects in our catalog. Light/narrower bars represent completeness-corrected values.

On the other side of the comparison, we identify four satellite candidates that are not included in the MATLAS catalog. These are SMDG1046186+115918, which is a satellite of NGC 3368, SMDG1155345+551658, which is a satellite of NGC 3972, and SMDG1504281+554100 and

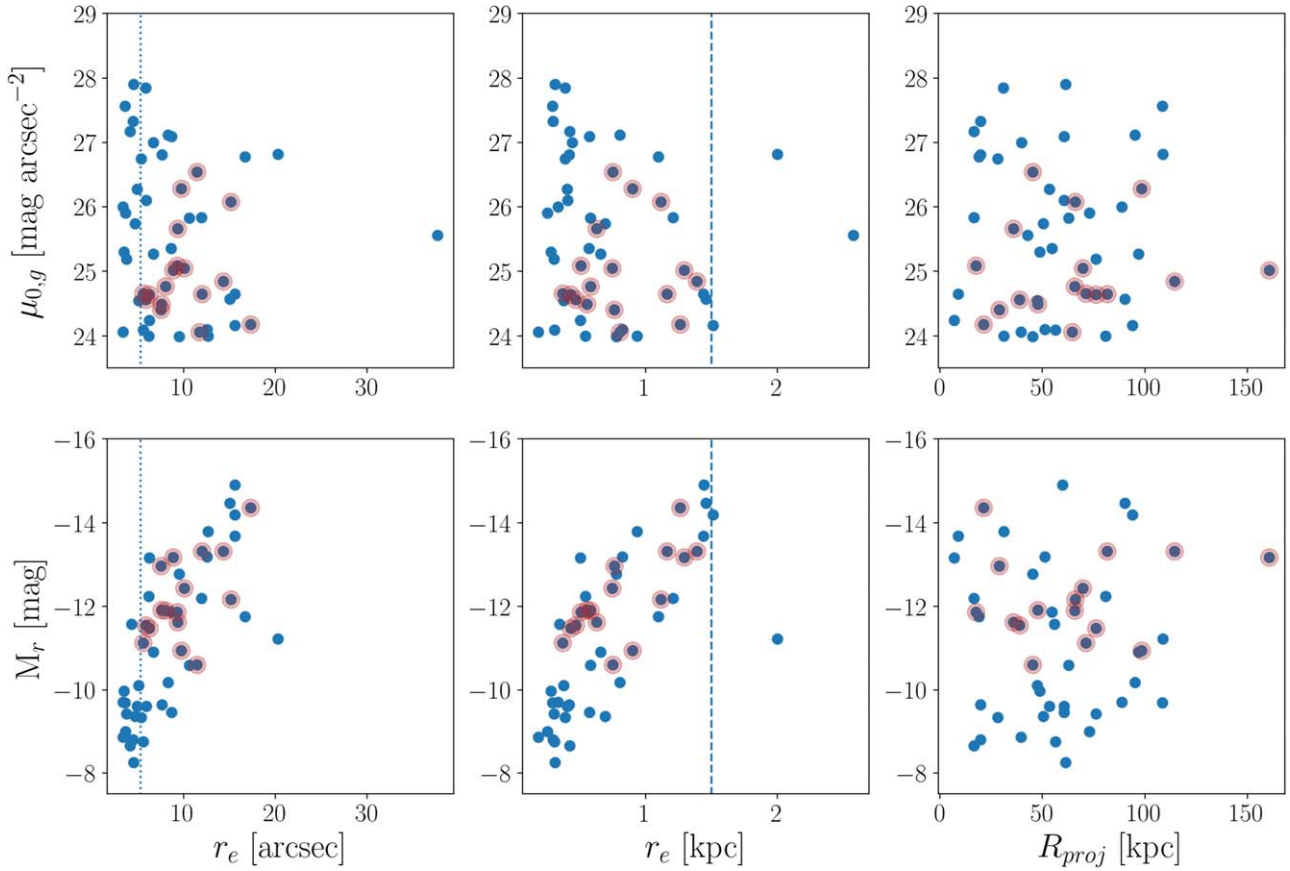

Figure 7. Distribution in satellite properties. Those galaxies also in the SMUDGes catalog (D. Zaritsky et al. 2023) are highlighted with larger, light red circles. Vertical lines in the first column of panels mark the SMUDGes minimum angular size criterion. The vertical lines in the middle panels mark the minimum physical size that defines the UDG category.

SMDG1508054+555216, which are satellites of NGC 5866. In two cases, $\mu_{0,g}$ is greater than 27 mag arcsec^{-2}, so these are challenging sources to identify and classify properly. The other two are in a parameter range where similar systems were successfully recovered in MATLAS, so the reason for their omission is less evident, although it could be an innocuous one, such as that the galaxy lies outside their survey footprint.

Our conclusion is that LIGHTS provides a dwarf galaxy sample at the lowest surface brightness that is comparable to the one provided by MATLAS, but generally for later-type parent galaxies. LIGHTS is therefore an excellent complement to MATLAS for those interested in comparing satellites across parents of differing morphologies.

6. Discussion

6.1. The Numbers of UDG Satellites versus Halo Mass

A number of studies aim to quantify the number of satellites, and in particular, low-surface-brightness and low-luminosity satellites per Milky Way analog (MWA; D. Zaritsky et al. 1997; M. Geha et al. 2017; P. Bennet et al. 2019; S. G. Carlsten et al. 2021; Y.-Y. Mao et al. 2021; J. Li et al. 2023; H. Goto et al. 2023). The most similar, in terms of technique and selection criteria, are those of J. Li et al. (2023) and H. Goto et al. (2023), who found that MWAs average 0.44 ± 0.05 and 0.5 ± 0.1 UDGs, respectively. In the H. Goto et al. (2023) study, MWAs were defined to have $-22 < M_g/\mathrm{mag} < -20$ (corresponding to $-22.5 < M_r/\mathrm{mag} < -20.5$ for the color of the Milky Way), the satellites were in the range $-17 < M_g/\mathrm{mag} < -13$, and the range of projected radii considered was $20 < R_{\mathrm{proj}}/\mathrm{kpc} < 250$. Our study focuses on lower-luminosity primaries, i.e., those that in the median are ∼1 mag fainter. It also extends to satellites with lower absolute magnitudes, which will not affect the UDG counts because the UDGs are relatively bright, but it does not reach out as far in projected radius.

We find three, possibly four UDGs if the one galaxy with $r_e = 1.46$ kpc (SMDG1222421+085000) is included. Although none of these were included in the SMUDGes catalog, one of these (SMDG1215038+473833) has extremely low central surface brightness >26.5 mag arcsec^{-2} and we would not expect SMUDGes to have included it. Two of these are in the NGC 4307 field (one is SMDG1222421+085000), which we previously noted we suspect of being in a group, and another is at $R_{proj} > 100$, where we are highly incomplete (this is also the one with very low central surface brightness). If we remove those in the NGC 4307 field and the one at large radius from consideration, we conclude that we find one UDG satellite candidate in the sample of 23 target galaxies (2.5 after photometric and radial completeness corrections), for a completeness-corrected frequency of 0.11 ± 0.11 candidate UDG satellites per host galaxy out to 100 kpc.

We now compare our result to that of H. Goto et al. (2023) for the relationship between UDGs and halo mass. Our primaries have a median magnitude of −20.6, which is ∼one mag fainter than the midpoint of the H. Goto et al. (2023) MWAs and hence a factor of 2.5 lower in stellar mass. At these stellar masses ($\log(M_*/M_\odot) \sim 10.3$), the galaxies lie near the

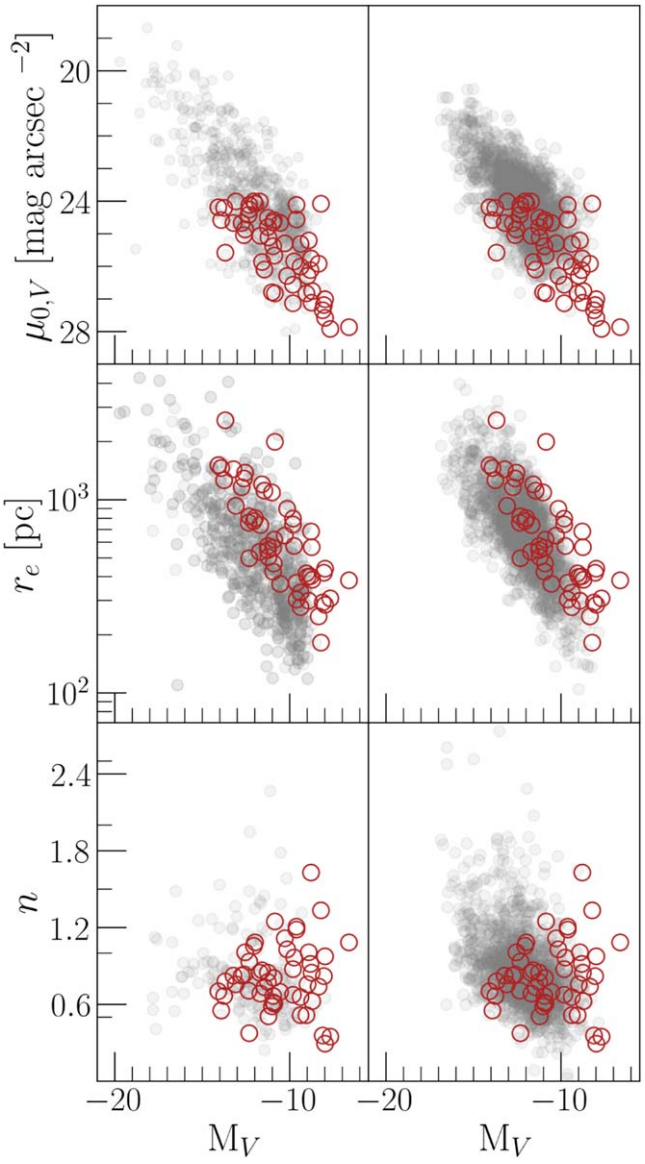

Figure 8. Comparison of properties of LIGHTS LSB satellites, open red circles, and a combination of data from the literature in filled gray circles. In the left panels, the literature sample consists of data from ELVES (S.G. Carlsten et al. 2022) and KMTNet (H. S. Park et al. 2017, 2019), while in the right panels, the literature data come from MATLAS (M. Poulain et al. 2021).

Table 5
LIGHTS LSB Satellites Matched to MATLAS Galaxies

SMDG Designation	MATLAS Designation
SMDG1046302+114522	MATLAS-740
SMDG1047059+115243	MATLAS-749
SMDG1047405+120258	MATLAS-753
SMDG1152340+370702	MATLAS-1111
SMDG1155406+552155	MATLAS-1120
SMDG1156093+551556	MATLAS-1124
SMDG1504500+553844	MATLAS-2006
SMDG1505300+555200	MATLAS-2026
SMDG1505523+553200	MATLAS-2043
SMDG1507165+552829	MATLAS-2084

knee of the stellar mass–halo mass relation, where M_*/M_h is roughly constant (Behroozi et al. 2010), and we adopt the approximation that the total mass-to-light ratio is comparable between our sample and that of the MWAs, resulting in the estimate that our sample has a halo mass that is 2.5× lower than that of the H. Goto et al. (2023) sample. For the relationship between halo mass and the number of UDGs presented in H. Goto et al. (2023) Figure 4 (from A. Karunakaran & D. Zaritsky 2023), we would then expect our galaxies to have 0.24 times as many UDG satellites within their virial radius as do MWAs.

Before we make the comparison to our measurement, we must account for the fact that we do not survey out to the virial radius. Because $r_{200} \propto M_{200}^{1/3}$, we expect the median virial radius of our galaxies to be ∼180 kpc instead of the 250 kpc of the H. Goto et al. (2023) sample. If the satellite galaxy number density profile is $\propto r^{-2}$ (which, as discussed, would be consistent with the data in Section 4), then we expect a factor of 100/180 UDGs when we confine ourselves to within 100 kpc, so the final expected number, extending the H. Goto et al. (2023) relationship, is 0.07 ± 0.01. This expectation is in agreement with our completion-corrected measurement of 0.11 ± 0.11 UDG satellites per host, and so we find no evidence for a deviation from the $N_{\rm UDG}$ − halo mass relation even when extending the relation to galaxies that are ∼1 mag fainter than MWAs.[14]

6.2. Nucleated Satellites

We visually identify, and present in Figure 9, 12 LSB satellite candidates that host nuclear star clusters (NSCs). In a couple of cases, the fields appear sufficiently crowded with unresolved sources that the NSC may instead be an unfortunate projection of an unassociated source (e.g., SMDG0240045-082646). In general, however, well-centered sources are exceedingly rare, and the vast majority of such sources are NSCs (see M. Lambert et al. 2024, in support of this claim at shallower imaging depth), so we proceed for now assuming that these are all associated. For a more quantitative estimate of the likelihood of a chance superposition in the LIGHTS data, we await the full source catalogs, from which we can measure the projected density of sources and assess the likelihood of a random source lying within any specific projected radius of the satellite galaxy center.

In the simplest comparison, not accounting for NSC incompleteness or relative depth and resolution differences among the samples, we compare our measurement of the NSC incidence (12/54 or 22%) with that of the MATLAS dwarfs (508/2210 or 23%; M. Poulain et al. 2021). Despite the difficulties in comparing across samples, the excellent agreement suggests that there are no gross differences either in the detection efficiencies nor in the physical properties of the galaxies themselves. The latter suggests that local environment, in terms only of being characterized as a satellite of an early- or late-type galaxy, may not play a strong role in defining the NSC occupation fraction.

7. Summary

We present the current status of the LIGHTS (LBT Imaging of Galactic Halos and Tidal Structures) survey, an overview of

[14] This comparison, as with any between satellite samples, needs to account for the fact that these are all carried out selecting in terms of *projected* radius (as stressed by H. Goto et al. 2023) and therefore includes galaxies at larger radii. Given the small number of galaxies being discussed here (i.e., one UDG), the additional complexity is not yet warranted, but this should still be noted.

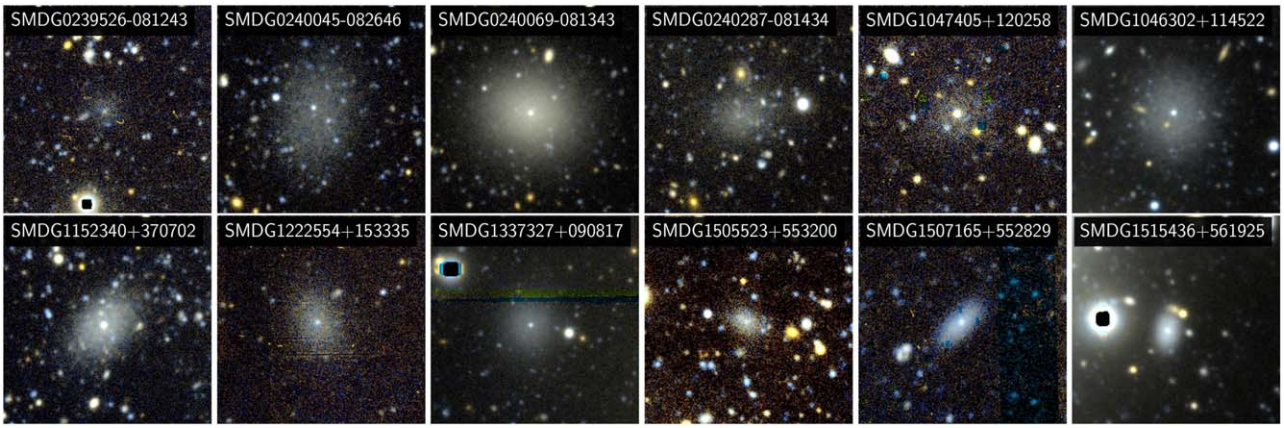

Figure 9. The 12 satellites galaxies identified visually to have nuclear star clusters. Square black regions indicate regions masked from the LIGHTS final images because they contain corrupted data. The images are ∼70″ on a side, and north is up.

the data processing and quality, and a catalog of low surface brightness ($\mu_{0,g} > 24$ mag arcsec^{-2}) satellite galaxy candidates.

Regarding the status, we now have deep g- and r-band imaging of 25 galaxies. The target galaxies are mostly morphologically late type and in the median about a magnitude fainter than our Milky Way galaxy. They span a range of environments, although mostly low-density ones, and were selected to be in low-extinction regions of the sky and relatively uncontaminated by bright stars. The extinction and low stellar contamination are essential to reaching the lowest possible surface brightness. The sample will grow slightly with time, but is mostly complete. The depth of the imaging will rival the full 10 yr depth of the LSST, and so it provides excellent guidance on what can be expected to become available across a large fraction of the observable sky.

We describe the data reduction process that enables us to consistently reach a 3σ r-band surface brightness in areas equivalent to 10″ boxes ∼30.5 mag arcsec^{-2} across the sample. In particular, we rely on an iterative masking and background modeling used to achieve the final sensitivity and state-of-the-art object extraction software in Gnuastro.

We make slight modifications to the low surface brightness object detection procedure outlined by D. Zaritsky et al. (2019, 2021, 2022, 2023) to generate a catalog of 54 low surface brightness satellite galaxy candidates. These are defined to have $\mu_{0,g} > 24$ mag arcsec^{-2} and $r_e > 3\farcs2$. Detections extend nearly to $\mu_{0,g} = 28$ mag arcsec^{-2}, which is ∼2 mag fainter than the same procedure reached on Legacy Survey images (A. Dey et al. 2019). We use simulated sources to derive completeness estimates across the parameter range covered by our detected sources. These candidates are mostly confined to within 100 kpc projected radius from their parent galaxy, due to the image size.

We expect, after applying the completeness corrections, that satellites of even lower total luminosity ($M_r > -10$ mag) and lower central surface brightness ($\mu_{0,r} > 27.5$ mag arcsec^{-2}) will be more prevalent. Over the parameter range we explore, each host (excluding those that are in overdense regions, apparently groups) has nearly four LSB satellites to a projected radius of 100 kpc. These objects are mostly just at or beyond the reach of spectroscopic surveys of LSB galaxies (e.g., J. Kadowaki et al. 2021) unless they are H I rich or have ongoing star formation. However, they are sufficiently close to us, if truly associated with their host galaxies, that other distance estimators utilizing resolved stars or the globular cluster luminosity function could be exploited with space-based observatories. For the fainter, smaller satellites that might have fewer luminous stars or globular clusters, even these methods may fail.

In our catalog, there are three, possibly four, ultra-diffuse galaxies (UDGs; $r_e > 1.5$ kpc). This allows us to explore and possibly extend the relationship between the number of UDGs and the host halo mass found for more massive systems (R. F. J. van der Burg et al. 2016; J. Roman & I. Trujillo 2017; P. E. Mancera Piña et al. 2019; A. Karunakaran & D. Zaritsky 2023; H. Goto et al. 2023). Despite differences in sample selection, we find that our results are in agreement with the extrapolation of the mean relationship used by A. Karunakaran & D. Zaritsky (2023) to galaxies that are a magnitude fainter than the Milky Way.

We visually identify 12 galaxies in our catalog that host a nuclear star cluster (NSC). The occupation fraction for the sample (12/54) is in excellent agreement with that found among satellites of early type galaxies (M. Poulain et al. 2021), and so suggests that the morphological type of the parent galaxy plays at most a limited role in the NSC satellite occupation fraction.

The LIGHTS sample provides exquisite data for the exploration of the halo stellar populations, whether they be diffusely distributed, in tidal features, or, as described here, still part of a low surface brightness satellite galaxy. Comparison with state-of-the-art published studies shows that LIGHTS matches or supersedes the sensitivity of those and/or provides data for a different category of parent galaxy. It is a resource for current study, but also provides direct guidance on the potential of upcoming deep imaging surveys such as the LSST that will be carried out using the Rubin telescope.

Acknowledgments

D.Z. acknowledges financial support from NSF AST-1713841 and AST-2006785. The authors thank the anonymous referee for a careful and thoughtful reading of the manuscript. An allocation of computer time from the UA Research Computing High Performance Computing (HPC) at the University of Arizona and the prompt assistance of the associated computer support group are also gratefully acknowledged. We acknowledge the usage of the HyperLeda database (http://leda.univ-lyon1.fr). I.T. acknowledges support from the ACIISI, Consejería de Economía, Conocimiento y Empleo del Gobierno de Canarias, and the European Regional

Development Fund (ERDF) under grant with reference PROID2021010044, and from the State Research Agency (AEI-MCINN) of the Spanish Ministry of Science and Innovation under the grant PID2022-140869NB-I00, as well as IAC project P/302302, financed by the Ministry of Science and Innovation, through the State Budget and by the Canary Islands Department of Economy, Knowledge and Employment, through the Regional Budget of the Autonomous Community. R.I.S. acknowledges funding by the Governments of Spain and Aragón through FITE and Science Ministry (PGC2018-097585-B-C21, PID2021-124918NA-C43). M.M. acknowledges support from the Project PCI2021-122072-2B, financed by MICIN/AEI/10.13039/501100011033, and the European Union "NextGenerationEU"/RTRP. J.R. acknowledges funding from University of La Laguna through the Margarita Salas Program from the Spanish Ministry of Universities ref. UNI/551/2021-May 26, and under the EU Next Generation.

Software: Astropy (Astropy Collaboration et al. 2013, 2018), astroquery (A. Ginsburg et al. 2019), Astrometry.net (D. Lang et al. 2010), GALFIT (C. Y. Peng et al. 2002), Gnuastro (M. Akhlaghi & T. Ichikawa 2015; M. Akhlaghi 2019), keras (F. Chollet & Keras Team 2015), lmfit (M. Newville et al. 2014), Matplotlib (J. D. Hunter 2007), NumPy (S. van der Walt et al. 2011), pandas (W. McKinney 2010), sep (K. Barbary 2016), Source Extractor (E. Bertin & S. Arnouts 1996), SCAMP (E. Bertin 2006), SciPy (T. E. Oliphant 2007; K. J. Millman & M. Aivazis 2011), SWarp (E. Bertin et al. 2002).

ORCID iDs

Dennis Zaritsky https://orcid.org/0000-0002-5177-727X
Giulia Golini https://orcid.org/0009-0001-2377-272X
Richard Donnerstein https://orcid.org/0000-0001-7618-8212
Ignacio Trujillo https://orcid.org/0000-0001-8647-2874
Mohammad Akhlaghi https://orcid.org/0000-0003-1710-6613
Nushkia Chamba https://orcid.org/0000-0002-1598-5995
Mauro D'Onofrio https://orcid.org/0000-0001-6441-9044
Sepideh Eskandarlou https://orcid.org/0000-0002-6672-1199
S. Zahra Hosseini-ShahiSavandi https://orcid.org/0000-0003-3449-2288
Raúl Infante-Sainz https://orcid.org/0000-0002-6220-7133
Garreth Martin https://orcid.org/0000-0003-2939-8668
Mireia Montes https://orcid.org/0000-0001-7847-0393
Javier Román https://orcid.org/0000-0002-3849-3467
Nafise Sedighi https://orcid.org/0009-0001-9574-8585
Zahra Sharbaf https://orcid.org/0009-0004-5054-5946

References

Akhlaghi, M. 2019, arXiv:1909.11230
Akhlaghi, M., & Ichikawa, T. 2015, ApJS, 220, 1
Amorisco, N. C. 2017, MNRAS, 464, 2882
Astropy Collaboration, Robitaille, T. P., Tollerud, E. J., et al. 2013, A&A, 558, A33
Astropy Collaboration, Price-Whelan, A. M., Sipőcz, B. M., et al. 2018, AJ, 156, 123
Barbary, K. 2016, JOSS, 1, 58
Behroozi, P. S., Conroy, C., & Wechsler, R. H. 2010, ApJ, 717, 379
Bennet, P., Sand, D. J., Crnojević, D., et al. 2019, ApJ, 885, 153
Bertin, E. 2006, in ASP Conf. Ser. 351, Astronomical Data Analysis Software and Systems XV, ed. C. Gabriel et al. (San Francisco, CA: ASP), 112
Bertin, E., & Arnouts, S. 1996, A&AS, 117, 393
Bertin, E., Mellier, Y., Radovich, M., et al. 2002, in ASP Conf. Ser. 281, The TERAPIX Pipeline, ed. D. A. Bohlender, D. Durand, & T. H. Handley (San Francisco, CA: ASP), 228
Bílek, M., Duc, P.-A., Cuillandre, J.-C., et al. 2020, MNRAS, 498, 2138
Bland-Hawthorn, J., & Gerhard, O. 2016, ARA&A, 54, 529
Blumenthal, G. R., Faber, S. M., Primack, J. R., & Rees, M. J. 1984, Natur, 311, 517
Bose, S., & Kumar, B. 2014, ApJ, 782, 98
Bullock, J. S., & Johnston, K. V. 2005, ApJ, 635, 931
Cantiello, M., Blakeslee, J., Raimondo, G., Brocato, E., & Capaccioli, M. 2007, ApJ, 668, 130
Carlsten, S. G., Greene, J. E., Beaton, R. L., & Greco, J. P. 2022, ApJ, 927, 44
Carlsten, S. G., Greene, J. E., Peter, A. H. G., Beaton, R. L., & Greco, J. P. 2021, ApJ, 908, 109
Chollet, F. & Keras Team 2015, Keras
Cooper, A. P., Cole, S., Frenk, C. S., et al. 2010, MNRAS, 406, 744
Danieli, S., van Dokkum, P., Abraham, R., et al. 2020, ApJL, 895, L4
Davis, A. B., Nierenberg, A. M., Peter, A. H. G., et al. 2021, MNRAS, 500, 3854
Davis, M., Efstathiou, G., Frenk, C. S., & White, S. D. M. 1985, ApJ, 292, 371
Dey, A., Schlegel, D. J., Lang, D., et al. 2019, AJ, 157, 168
Duc, P.-A., Cuillandre, J.-C., Karabal, E., et al. 2015, MNRAS, 446, 120
Eskandarlou, S., Akhlaghi, M., Infante-Sainz, R., et al. 2023, RNAAS, 7, 269
Fan, T. J., Moon, D.-S., Park, H. S., et al. 2023, MNRAS, 525, 4904
Font, A. S., McCarthy, I. G., Crain, R. A., et al. 2011, MNRAS, 416, 2802
Forbes, D. A., Gannon, J., Couch, W. J., et al. 2019, A&A, 626, A66
Freedman, W. L., Madore, B. F., Gibson, B. K., et al. 2001, ApJ, 553, 47
Fukugita, M., Shimasaku, K., & Ichikawa, T. 1995, PASP, 107, 945
Gaia Collaboration, Brown, A. G. A., Vallenari, A., et al. 2021, A&A, 649, A1
Geha, M., Wechsler, R. H., Mao, Y.-Y., et al. 2017, ApJ, 847, 4
Giallongo, E., Ragazzoni, R., Grazian, A., et al. 2008, A&A, 482, 349
Ginsburg, A., Sipőcz, B. M., Brasseur, C. E., et al. 2019, AJ, 157, 98
Gonzalez, A. H., Zaritsky, D., Dalcanton, J. J., & Nelson, A. 2001, ApJS, 137, 117
Goto, H., Zaritsky, D., Karunakaran, A., Donnerstein, R., & Sand, D. J. 2023, AJ, 166, 185
Hodge, P. W. 1983, PASP, 95, 721
Hoffleit, D., & Warren, W. H. J. 1995, yCat, V/50
Hunter, J. D. 2007, CSE, 9, 90
Infante-Sainz, R., & Akhlaghi, M. 2024, RNAAS, 8, 10
Jacobs, B. A., Rizzi, L., Tully, R. B., et al. 2009, AJ, 138, 332
Ji, A. P., Koposov, S. E., Li, T. S., et al. 2021, ApJ, 921, 32
Johnston, K. V., Bullock, J. S., Sharma, S., et al. 2008, ApJ, 689, 936
Jones, E., Oliphant, T., P. P., et al. 2001, SciPy: Open Source
Kadowaki, J., Zaritsky, D., Donnerstein, R., et al. 2021, ApJ, 923, 257
Karunakaran, A., & Zaritsky, D. 2023, MNRAS, 519, 884
Karunakaran, A., Spekkens, K., Oman, K. A., et al. 2021, ApJL, 916, L19
Kennicutt, R. C. J. 2001, in ASP Conf. Ser. 231, Tetons 4: Galactic Structure, Stars and the Interstellar Medium, ed. C. E. Woodward, M. D. Bicay, & J. M. Shull (San Francisco, CA: ASP), 2
Koda, J., Yagi, M., Yamanoi, H., & Komiyama, Y. 2015, ApJL, 807, L2
Kourkchi, E., & Tully, R. B. 2017, ApJ, 843, 16
Kourkchi, E., Tully, R. B., Eftekharzadeh, S., et al. 2020, ApJ, 902, 145
Lambert, M., Khim, D. J., Zaritsky, D., & Donnerstein, R. 2024, AJ, 167, 61
Lang, D., Hogg, D. W., Mierle, K., Blanton, M., & Roweis, S. 2010, AJ, 139, 1782
Li, J., Greene, J. E., Greco, J. P., et al. 2023, ApJ, 955, 1
Makarov, D., Prugniel, P., Terekhova, N., Courtois, H., & Vauglin, I. 2014, A&A, 570, A13
Mancera Piña, P. E., Aguerri, J. A. L., Peletier, R. F., et al. 2019, MNRAS, 485, 1036
Mao, Y.-Y., Geha, M., Wechsler, R. H., et al. 2021, ApJ, 907, 85
Martin, G., Bazkiaei, A. E., Spavone, M., et al. 2022, MNRAS, 513, 1459
McKinney, W. 2010, in Proc. 9th Python in Sci. Conf., Vol. 51 (Austin, TX: SciPy)
Merritt, A., Pillepich, A., van Dokkum, P., et al. 2020, MNRAS, 495, 4570
Merritt, A., van Dokkum, P., Abraham, R., & Zhang, J. 2016, ApJ, 830, 62
Millman, K. J., & Aivazis, M. 2011, CSE, 13, 9
Monelli, M., & Trujillo, I. 2019, ApJL, 880, L11
Moustakas, J., Lang, D., Dey, A., et al. 2023, ApJS, 269, 3
Müller, O., & Jerjen, H. 2020, A&A, 644, A91
Naidu, R. P., Conroy, C., Bonaca, A., et al. 2020, ApJ, 901, 48
Nashimoto, M., Tanaka, M., Chiba, M., et al. 2022, ApJ, 936, 38
Nasonova, O. G., de Freitas Pacheco, J. A., & Karachentsev, I. D. 2011, A&A, 532, A104
Neumayer, N., Seth, A., & Böker, T. 2020, A&ARv, 28, 4

Newville, M., Stensitzki, T., Allen, D. B., & Ingargiola, A. 2014, LMFIT: Non-Linear Least-Square Minimization and Curve-Fitting for Python, v1.3.1, Zenodo, doi:10.5281/zenodo.11813
Oke, J. B. 1964, ApJ, 140, 689
Oke, J. B., & Gunn, J. E. 1983, ApJ, 266, 713
Oliphant, T. E. 2007, CSE, 9, 10
Park, H. S., Moon, D.-S., Zaritsky, D., et al. 2019, ApJ, 885, 88
Park, H. S., Moon, D.-S., Zaritsky, D., et al. 2017, ApJ, 848, 19
Pedregosa, F., Varoquaux, G., Gramfort, A., et al. 2011, JMLR, 12, 2825
Peng, C. Y., Ho, L. C., Impey, C. D., & Rix, H.-W. 2002, AJ, 124, 266
Poulain, M., Marleau, F. R., Habas, R., et al. 2021, MNRAS, 506, 5494
Riess, A. G., Macri, L. M., Hoffmann, S. L., et al. 2016, ApJ, 826, 56
Roman, J., & Trujillo, I. 2017, MNRAS, 468, 4039
Santos-Santos, I. M. E., Sales, L. V., Fattahi, A., & Navarro, J. F. 2022, MNRAS, 515, 3685
Schlegel, D. J., Finkbeiner, D. P., & Davis, M. 1998, ApJ, 500, 525
Shaya, E. J., Tully, R. B., Hoffman, Y., & Pomarède, D. 2017, ApJ, 850, 207
Sola, E., Duc, P.-A., Richards, F., et al. 2022, A&A, 662, A124
Szabo, T., Pierpaoli, E., Dong, F., Pipino, A., & Gunn, J. 2011, ApJ, 736, 21
Torrealba, G., Belokurov, V., Koposov, S. E., et al. 2019, MNRAS, 488, 2743
Trujillo, I., & Fliri, J. 2016, ApJ, 823, 123
Trujillo, I., Beasley, M. A., Borlaff, A., et al. 2019, MNRAS, 486, 1192
Trujillo, I., D'Onofrio, M., Zaritsky, D., et al. 2021, A&A, 654, A40
Tully, R. B., Courtois, H. M., & Sorce, J. G. 2016, AJ, 152, 50
Tully, R. B., Courtois, H. M., Dolphin, A. E., et al. 2013, AJ, 146, 86
van der Burg, R. F. J., Muzzin, A., & Hoekstra, H. 2016, A&A, 590, A20
van der Walt, S., Colbert, S. C., & Varoquaux, G. 2011, CSE, 13, 22
van Dokkum, P., Abraham, R., Romanowsky, A. J., et al. 2017, ApJL, 844, L11
van Dokkum, P. G., Abraham, R., & Merritt, A. 2014, ApJL, 782, L24
van Dokkum, P. G., Abraham, R., Merritt, A., et al. 2015, ApJL, 798, L45
Weinberg, D. H., Bullock, J. S., Governato, F., Kuzio de Naray, R., & Peter, A. H. G. 2015, PNAS, 112, 12249
Xi, C., Taylor, J. E., Massey, R. J., et al. 2018, MNRAS, 478, 5336
Zaritsky, D. 2017, MNRAS, 464, L110
Zaritsky, D., Donnerstein, R., Dey, A., et al. 2023, ApJS, 267, 27
Zaritsky, D., Donnerstein, R., Karunakaran, A., et al. 2022, ApJS, 261, 11
Zaritsky, D., Donnerstein, R., Karunakaran, A., et al. 2021, ApJS, 257, 60
Zaritsky, D., Smith, R., Frenk, C., & White, S. D. M. 1997, ApJ, 478, 39
Zaritsky, D., Donnerstein, R., Dey, A., et al. 2019, ApJS, 240, 1